nature nanotechnology

Article

https://doi.org/10.1038/s41565-022-01291-1

Achieving nanoscale precision using neuromorphic localization microscopy

Received: 11 November 2021

Accepted: 9 November 2022

Published online: 23 January 2023

Check for updates

Rohit Mangalwedhekar[1], Nivedita Singh[1], Chetan Singh Thakur[2], Chandra Sekhar Seelamantula[3], Mini Jose[1] & Deepak Nair[1]

Neuromorphic cameras are a new class of dynamic-vision-inspired sensors that encode the rate of change of intensity as events. They can asynchronously record intensity changes as spikes, independent of the other pixels in the receptive field, resulting in sparse measurements. This recording of such sparse events makes them ideal for imaging dynamic processes, such as the stochastic emission of isolated single molecules. Here we show the application of neuromorphic detection to localize nanoscale fluorescent objects below the diffraction limit, with a precision below 20 nm. We demonstrate a combination of neuromorphic detection with segmentation and deep learning approaches to localize and track fluorescent particles below 50 nm with millisecond temporal resolution. Furthermore, we show that combining information from events resulting from the rate of change of intensities improves the classical limit of centroid estimation of single fluorescent objects by nearly a factor of two. Additionally, we validate that using post-processed data from the neuromorphic detector at defined windows of temporal integration allows a better evaluation of the fractalized diffusion of single particle trajectories. Our observations and analysis is useful for event sensing by nonlinear neuromorphic devices to ameliorate real-time particle localization approaches at the nanoscale.

Naturally occurring phenomena are evaluated by paradigms that detect and classify signals into temporal sequences of defined patterns[1,2]. These approaches rely on integrating signals over a defined period that cannot be altered post recording of the phenomena. Over the past decade, recording stochastic events such as single molecule emission and tracking of subdiffraction-sized objects have become fundamental tools to understand self-organization and molecular order in different cellular compartments[3–8]. Image detectors such as electron-multiplying charge coupled devices (EMCCDs) and scientific complementary metal–oxide–semiconductor devices have been used to localize molecules with nanometre precision in real time[4,9–11]. Recently, a novel class of detectors based on the principle of neuromorphic sensing has been developed based on the dynamic visual perception of spatiotemporal stimuli[12–19]. In contrast to the uniform sampling used in integrative approaches, neuromorphic detectors rely on an event-driven detection by acquiring differential measurements of stimuli akin to the processing of sensory information by the brain[20–22]. In a neuromorphic camera, each pixel generates a spike event asynchronously based on the intensity change in its receptive field with very high temporal resolution on the order of a few microseconds, which makes these cameras an ideal choice for imaging dynamic processes[14,20,23]. The stochastic emission of sparse single molecules and rapid calculation of their centroids have become the paradigm of choice to localize subdiffraction-sized single fluorescent particles at a resolution of a few tens of nanometres[4,24,25]. The error in calculating the centroids of single molecule emission determines the resolution of the super-resolved image[3,4]. Paradigms relying on the stochastic emission of fluorescence signals are limited by the bandwidth of the detectors recording the

[1]Centre for Neuroscience, Indian Institute of Science, Bangalore, India. [2]Department of Electronic Systems Engineering, Indian Institute of Science, Bangalore, India. [3]Department of Electrical Engineering, Indian Institute of Science, Bangalore, India. e-mail: deepak@iisc.ac.in

sparse and intermittent nature of fluorescence[12,26,27]. We demonstrate that neuromorphic detection coupled with segmentation approaches or convolution neural network (CNN)-based deep learning allows the precise determination of centroids with an accuracy on the order of a few tens of nanometres. We demonstrate that the localization precision can be improved by combining information from the rates of both the increase and decrease in the intensity of the subdiffraction-sized fluorescent particles. Additionally, we demonstrate the suitability of neuromorphic sensors to detect point objects undergoing Brownian diffusion, which are classified based on their vectorial nature and confinement of movement. We also evaluate the fractalized nature of diffusion at a user-defined temporal sampling from the corresponding neuromorphic data.

Neuromorphic devices detect true nature of events

The images of single fluorescent particles of 100 nm were collected either by a neuromorphic camera (referred to as NM) or by an EMCCD (referred to as EM). The frame rate of acquisition of EM was synchronized with the illumination period of the laser. The EM image stack comprised alternating frames with particles displaying high- and low-intensity fluorescence, corresponding to the Hi and Lo states of the laser, respectively (Fig. 1a, EM). The events detected by NM were reconstructed into alternating frames of ON and OFF events of particles (Fig. 1a, NM). The total number of ON and OFF events were the same, confirming a spatial correlation of immobilized particles and events of opposing polarity (Fig. 1b,c). This ability of neuromorphic detection to discriminate signals allows one to recreate events at different temporal windows at user-defined frame rates, post acquisition. NM events were thus reconstructed into various user-defined intervals of integration of 100 ms, 50 ms, 25 ms and 10 ms, while the switching period of the laser was maintained at 100 ms (Fig. 1d). As the interval of integration was reduced, the signals were preferentially detected in the frames where the fluorescence emission of the particle alternated between the Hi and Lo states. As the interval of integration of events was decreased, the frames that followed laser switching to Hi or Lo states recorded the highest pixel intensity correlating with the sharpest changes (Fig. 1d). A workflow was implemented to evaluate the scheme for imaging and spatiotemporal analysis of single fluorescent particles using deep learning in the NM or EM modes (Extended Data Fig. 1).

To evaluate the fidelity of NM to record the true nature of events, we investigated the temporal correlation of ON and OFF events by differential sampling of polarity. We separated the data into two temporal stacks of positive and negative polarities representing ON and OFF events, respectively. The results confirmed that ON events were recorded when the illumination intensity increased, while OFF events were recorded during a decrease in intensity (Fig. 2a). The complementary polarities of the ON and OFF events enabled the robust synchronous temporal separation of events (Fig. 2a). We then evaluated the same data for the Hi and Lo states of the laser illumination, encompassing a full period of detection (Fig. 2b). We observed that a change in the magnitude of the positive or negative polarity from minima to maxima correlated with half the period, corresponding to the switching rate of the lasers. A fast Fourier transform (FFT) of the event sequences confirmed a switching period of 200 ms. This included the total time taken for a single Hi and Lo state of the laser (Fig. 2c). The integrated polarity and its period behaved similarly to a full recording of the ON and OFF processes upon illumination by the Hi and Lo states of the laser (Fig. 2d,e). The integrated intensity was proportional to the true intensity of the fluorescent particle and not to the Hi/Lo state of the laser. The particles consistently displayed the highest fluorescence at the end of the Hi state of the laser and the lowest fluorescence at the end of the Lo state, as indicated in a single period (Fig. 2g,h). The FFT of the integrated polarity and integrated intensity displayed a peak-to-peak interval of around 200 ms or 5 Hz, consistent with the switching period of the laser (Fig. 2f,i). Harmonics were also present, especially for the individual polarities and integrated polarity. The positive and negative polarities were offset by a phase of ~0.9π, signifying only a residual overlap of the ON and OFF events for a period of ~10 ms (Supplementary Table 1a–c). We confirmed that the overlap was independent of the switching period or frame rates of the detector, verifying that NM devices can indeed record the true nature of events (Supplementary Table 1a–c).

Comparison of neuromorphic devices to EMCCDs

NM detectors are optimized for imaging dynamic events in natural bright-light conditions. By contrast, EM is suited for sensing ultra-low levels of light, enabling the recording of emission from single fluorescent molecules, aided by their electron-multiplying gain. Since NM lacks the EM gain feature, we relied on switching the power levels of the laser to achieve an increase in the detected signal, whose amplitude is measured by the rate of change of the recorded emission of photons from a minimum to the maximum. The laser illumination power for EM detection was calibrated using 100 nm TetraSpeck beads to obtain the highest dynamic range at an EM gain of 500(Extended Data Fig. 2a). The same beads were then imaged at decreasing EM gains (Extended Data Fig. 2a). We observed that as the EM gain decreased, the dynamic range of the detection of EM decreased rapidly (Extended Data Fig. 2a). At the laser power for the maximum dynamic range of EM, NM displayed a dynamic range of 14–15 bit (2^{14}–2^{15}), which was close to that acquired using 50–100 EM gain (Extended Data Fig. 2b). It is well known that a reduction of the integration time at the same power reduces the dynamic range of the detected signal in EM. By contrast, alteration of the switching period of the laser did not result in a change of the dynamic range of detection for NM (Extended Data Fig. 2b). These observations confirmed that NM records the instantaneous rate of change of intensity and is dependent only on the temporal difference in emission. We repeated the experiments with reduced illumination power, confirming that the recording of events is dependent on the absolute maximum radiance of the emitted particle (Extended Data Fig. 2b). Additionally, when the NM sensors were compared across ON and OFF processes, there was no substantial change in the dynamic range of detection, confirming that processes were detected with comparable efficiencies (Extended Data Fig. 2c).

It is well understood that centroid estimation algorithms based on fitting using a Gaussian function or a wavelet rely on the signal-to-noise ratio (SNR) of the detected molecules along with the dynamic range of the detected signal[28,29]. As expected, at high illumination intensities, the localization precision and SNR in EM saturated quickly (Extended Data Fig. 3a,c and Supplementary Table 2a), and the localization precision did not show an improvement in pointing accuracy after the SNR increased to 50% of the saturated values (Extended Data Fig. 3a and Supplementary Table 2a). When the illumination power was as low as 10% of the original input power, we observed an improvement for both SNR and localization precision (Extended Data Fig. 3c and Supplementary Table 2a). Similarly, the localization precision and SNR for the detected events in NM were calculated by obtaining the intensity maxima of isolated single particles for corresponding ON/OFF processes and dividing these intensity maxima by the maximum of a randomly selected region where no events were recorded (Extended Data Fig. 3b,d and Supplementary Table 2b). The minimum in the same regions could not be used for calculating the SNR because of the detection method employed in NM, where the rate of change in intensity in many pixels was close to zero, resulting in anomalously large SNRs. Though we expected NM to have a localization precision and SNR similar to the data with the lowest EM gain (gain of 1) in similar conditions (100 ms integration for both EM and NM), NM performed similarly to EM with an EM gain in the range of 5–10 (Extended Data Fig. 3b,d).

https://doi.org/10.1038/s41565-022-01291-1

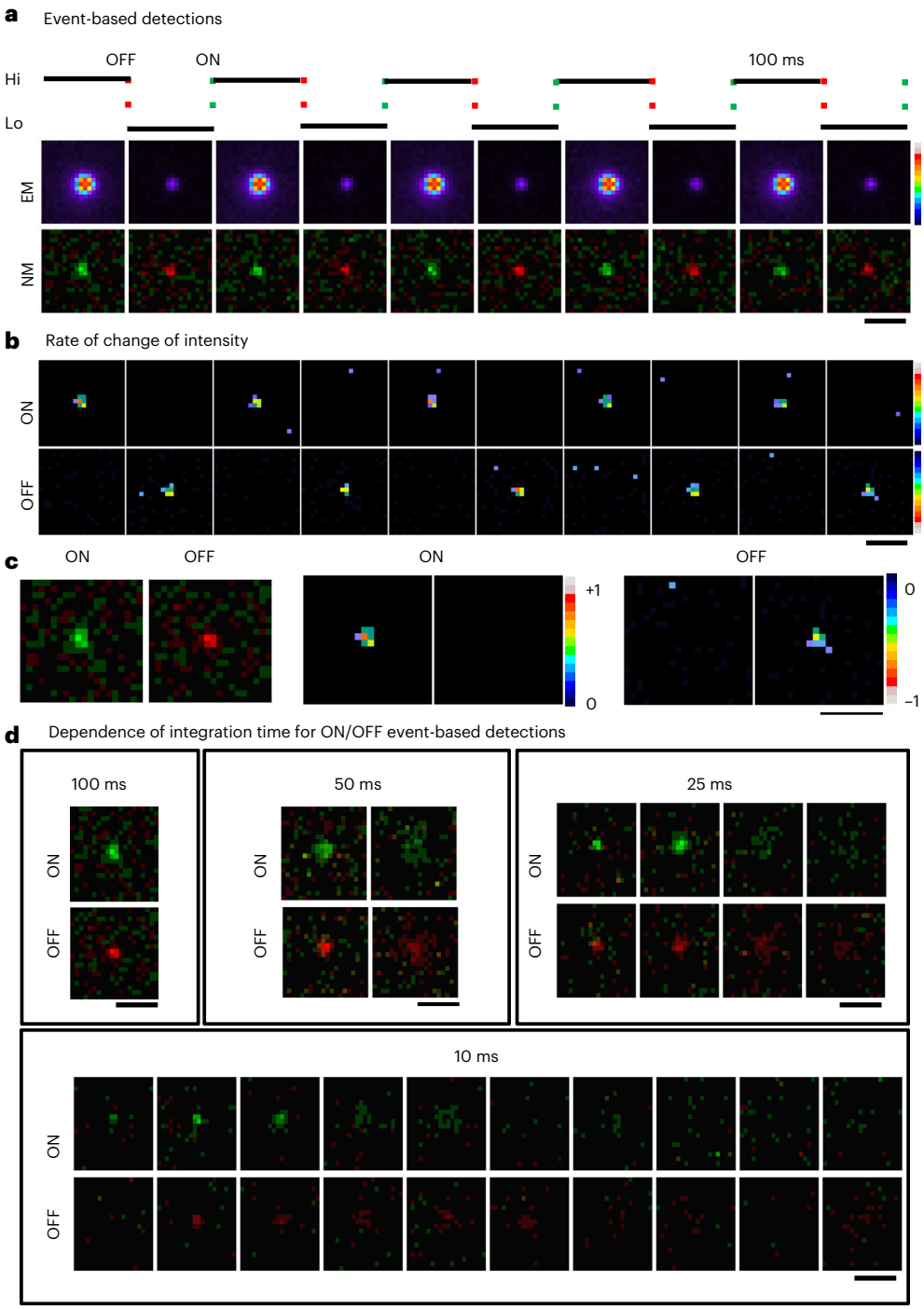

Fig. 1 | Detection of an isolated subdiffraction-sized single fluorescent particle using neuromorphic imaging. a, Comparison of the integrated detection of centroids of immobilized subdiffraction-sized fluorescent beads illuminated by a 647 nm laser using EM and NM. The frame rate of acquisition of EM was synchronized with the illumination period of the laser (referred to as the switching period) of 100 ms. The images were acquired continuously with the excitation laser intensity alternating between 100% laser power (Hi) and 10% laser power (Lo), as depicted by the waveform. Red indicates the beginning of the OFF process (Lo) and green indicates the beginning of ON process (Hi). Pseudo-colour intensity map for EM indicates maximum (white) and minimum (black) and intensities in between. Each image in the stream was integrated for 100 ms. The intensity fluctuation of a single particle is depicted as a pseudo-coloured intensity map (from top to bottom). The NM images are presented as a relative change in intensity, where green indicates an increase in signal (positive polarity), while red indicates the relative decrease in signal (negative polarity) for ON and OFF modes, respectively. **b**, Comparison of the rate of change of intensity in the NM detector between the ON and OFF processes for positive and negative polarities. Scale bars in **a** and **b**, 3.5 µm. **c**, Gallery of a single fluorescent particle switching between the Hi and Lo states in NM detection mode and the pseudo-colour intensity map for the polarity changes in the positive and negative channels. Scale bar, 3.5 µm. **d**, Event-based detection of ON and OFF events accumulated at different temporal resolutions on the neuromorphic detector. The Hi/Lo state for a single fluorescent particle was accumulated at different temporal samplings defined by the integration of events into a user-defined frame rate. Once the temporal resolution was increased, the ON (green) and OFF (red) processes were split across different time frames. Upon saturation, only residual changes in the intensity for the ON process were observed, highlighting the innate nature of event-based sensing in NM detectors. Scale bars, 3.5 µm.

https://doi.org/10.1038/s41565-022-01291-1

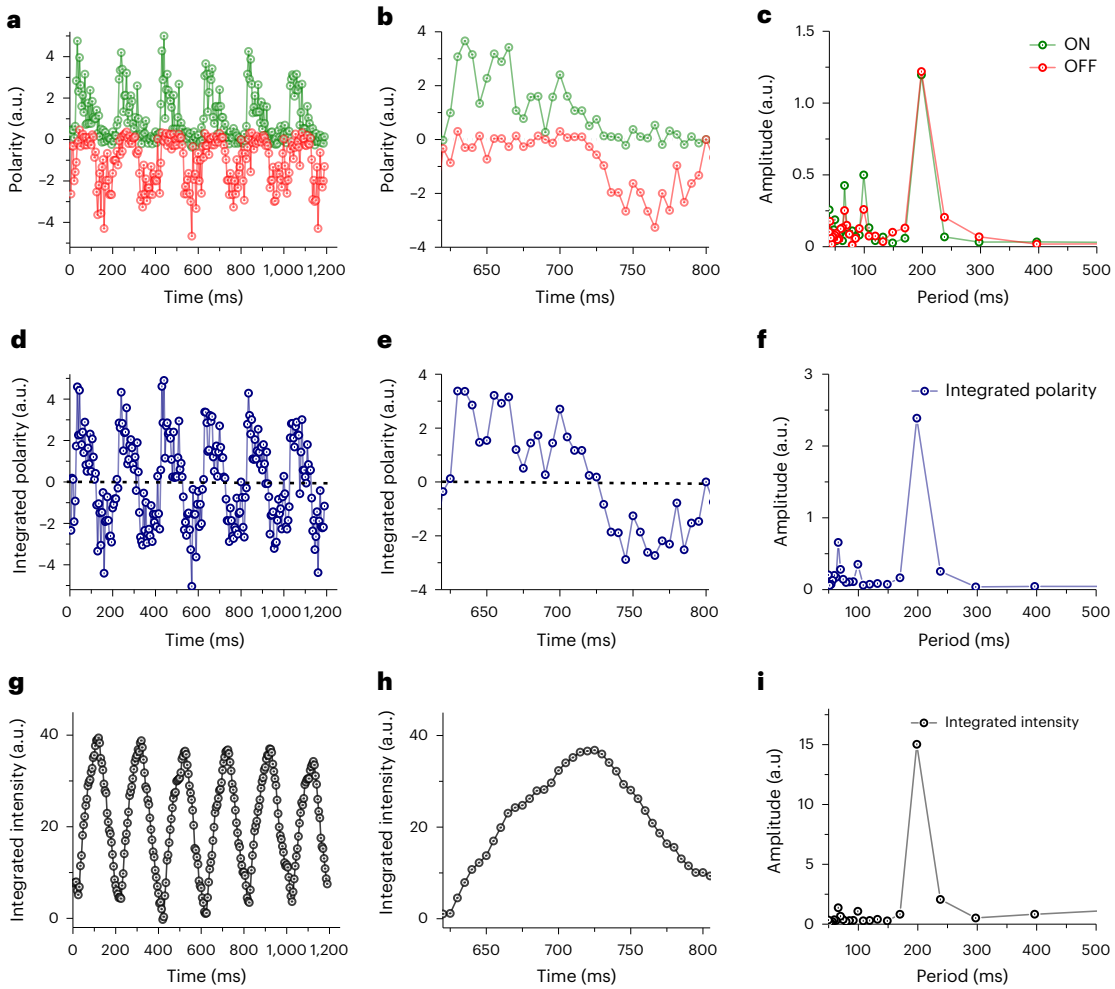

Fig. 2 | Temporal characteristics of emission of an isolated subdiffraction-sized single fluorescent particle using neuromorphic imaging. a, Positive (green) and negative (red) polarity indicating the ON and OFF processes, respectively, of a single fluorescent bead imaged by NM and accumulated at a resolution of 5 ms. The polarities are inversely correlated, where one reaches a high when the other is at a low and vice versa. Single particles are defined by a spatial window (region of interest) of 25 × 25 pixels to evaluate the temporal fluctuations in the greyscale values of the particle for the ON and OFF processes. **b**, Intensities corresponding to positive (green) and negative (red) polarities across a single ON and OFF period of the laser. The intensities of positive (green) and negative (red) polarities were offset by ~0.9π radians. **c**, The period of oscillation in intensity for positive (green) and negative (red) polarities was determined by performing a FFT. Both channels showed a large peak at ~200 ms, which is the total time for one Hi phase and one Lo phase of the laser. Additional smaller harmonics were also present at 100 ms and at 66 ms. **d**, Integrated polarity (navy blue) of a single fluorescent bead calculated as a summation of the positive and negative polarities at each time point. **e**, Integrated polarity intensities over a single ON and OFF period of the laser. **f**, The period of oscillation of the integrated polarity intensity was determined to be ~200 ms using a FFT in Origin. Additional harmonic peaks were also present at 100 ms and 66 ms. **g**, Integrated intensity (black) of a single fluorescent bead, determined as a cumulative sum from one time point to the next, followed a near sinusoidal waveform with a period of 200 ms. **h**, Integrated intensity over a single ON period (rising edge, corresponding to the integration of the net positive polarities) and a single OFF period (falling edge, corresponding to the integration of the net negative polarities) of a single fluorescent bead. **i**, The period of oscillation of the integrated intensity was determined to be ~200 ms using a FFT in Origin. Additional peaks were present at 100 ms and 66 ms.

Nonlinear detection of events improves estimation of localization precision

We observed that among all the parameters, a change in SNR had the most observable effect on the dataset for centroid estimation, consistent with previous reports using either deep learning methods or wavelet segmentation protocols[28–30] (Extended Data Figs. 3 and 4 and Supplementary Table 2a,b). Additionally, when we compared the SNR of EM at high and low illumination intensities, NM outperformed EM in noisy environments, as indicated by the performance at low illumination intensities for similar conditions of EM gain (Extended Data Fig. 3e,f and Supplementary Table 2a,b). At high and low illumination powers, the SNR and localization precision in NM improved with the switching period of the laser between ON and OFF processes as well as with the illumination intensities (Extended Data Fig. 3e,f and Supplementary Table 2a,b). These observations indicate that although the described NM is one of the first-generation detectors without any additional on-chip multiplication factor, which is different from the advanced sensor technology in EM, it is on par with EM with its inherent gain function. In short, the dynamic range and SNR of NM in all conditions worked better than EM at its lowest gain. The localization precision of NM was comparable to EM at the lowest gain with high illumination powers but outperformed EM when the SNRs were compared at noisier, weak-illumination conditions.

Next, we evaluated the suitability of NM to localize objects below the diffraction limit using deep learning[30]. We simulated a gallery of NM and EM images using DeepTrack and calculated the root mean square error in fitting the centroid of single particles with respect to the ground truth (Extended Data Fig. 4a,b). For event detection data

https://doi.org/10.1038/s41565-022-01291-1

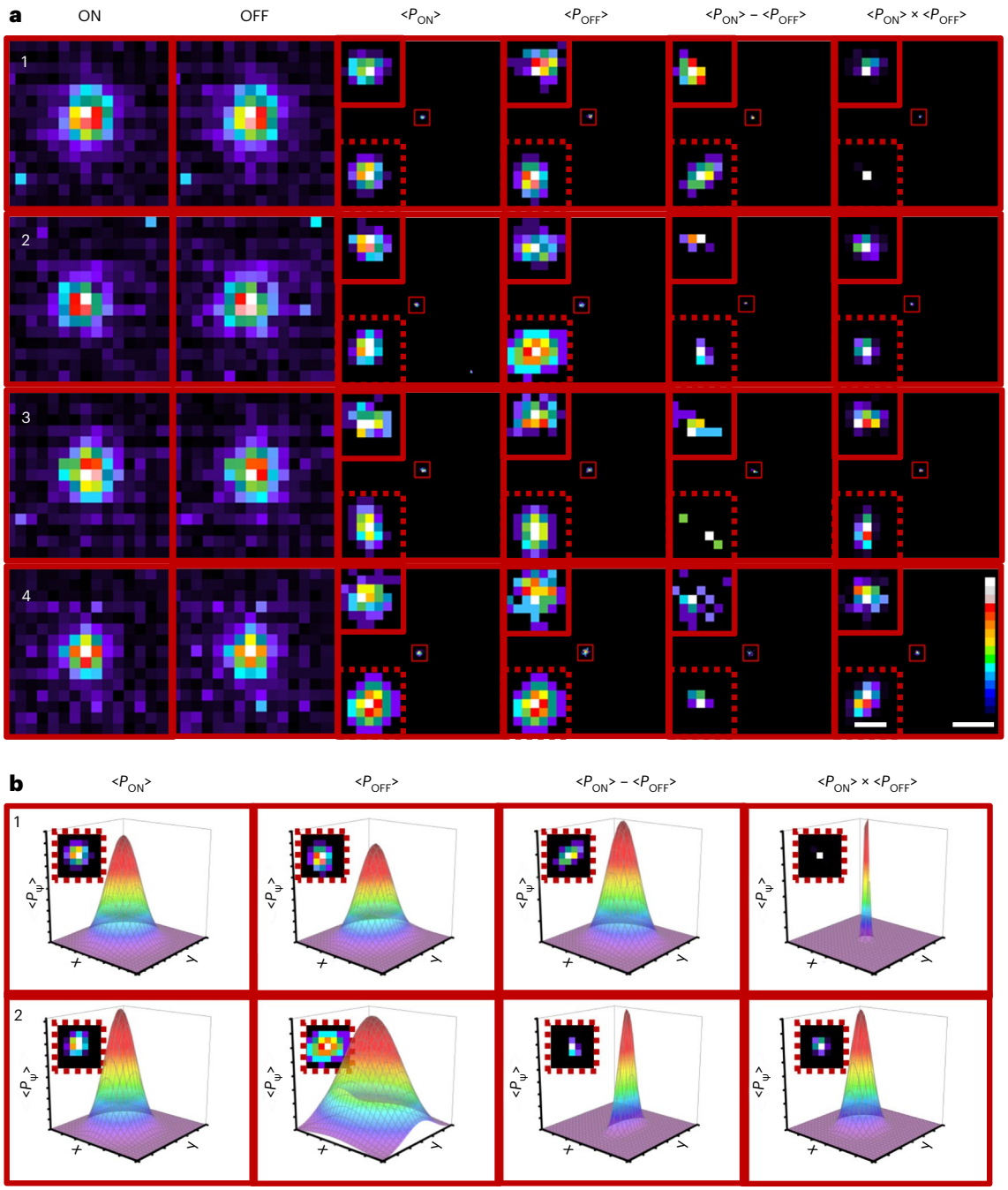

Fig. 3 | Transformation of cumulative probability density of ON and OFF processes allows localization below the limit of classical single particle detection. a, Gallery of single molecule localization and calculation of the PDF of the centroid from four subdiffraction-limited fluorescence particles with varying intensities using PalmTracer. ON and OFF indicates the nonlinearly and independently recorded raw ON and OFF events for the same molecule at a sampling of 185 nm per pixel. $\langle P_{ON}\rangle$ and $\langle P_{OFF}\rangle$ indicate the raw PDFs of centroids normalized to (0, 0) for the ON and OFF processes, respectively. $\langle P_{ON}\rangle - \langle P_{OFF}\rangle$ is the difference between $\langle P_{ON}\rangle$ and $\langle P_{OFF}\rangle$, whereas $\langle P_{ON}\rangle \times \langle P_{OFF}\rangle$ is the product of $\langle P_{ON}\rangle$ and $\langle P_{OFF}\rangle$. The top red (continuous) inset represents the raw PDF, and the bottom red (dotted) inset represents the same molecule after a 2D Gaussian fitting. All the images are normalized to maximum (white) to minimum (black), and the pseudo-colour bar represents the intensities in between in absolute units (a.u.) between the maxima and minima. Scale bar, 700 nm (70 nm for inset). Positive (green) and negative (red) polarities indicate the ON and OFF processes of a single fluorescent bead. Sampling of reconstructed centroids was at 18.5 nm per pixel. **b**, Gallery of raw and derived PDFs of ON and OFF processes of particles 1 (top row) and 2 (bottom row). The PDF is modelled by a 2D Gaussian for $\langle P_{ON}\rangle$, $\langle P_{OFF}\rangle$, $\langle P_{ON}\rangle - \langle P_{OFF}\rangle$ and $\langle P_{ON}\rangle \times \langle P_{OFF}\rangle$. In contrast to the raw $\langle P_{ON}\rangle$ and $\langle P_{OFF}\rangle$, the derived $\langle P_{ON}\rangle - \langle P_{OFF}\rangle$ and $\langle P_{ON}\rangle \times \langle P_{OFF}\rangle$ were observed to be isotropic when modelled as a function in 2D. The *X* and *Y* ranges of the plots are consistent with the inset size (130 nm) shown in **a**, and the inset is reproduced here. P_ψ is the probability density function of the particle for ON, OFF, the difference of ON and OFF, and the product of ON and OFF.

using NM, a comparable SNR at the experimental conditions (SNR, 6–8; ON events; 150 to 300 mW laser power; Supplementary Table 2b) was used to generate simulated data. In this case, the root mean square error values between the ground truth and localized fit based on the Nyquist criterion for sampling diffraction-limited objects were calculated to be 35.10 ± 10.80 nm and 25.20 ± 13.50 nm in the principal and auxiliary axes, respectively (Extended Data Fig. 4b). In similar experimental conditions, the NM localization precision of ON and OFF processes

https://doi.org/10.1038/s41565-022-01291-1

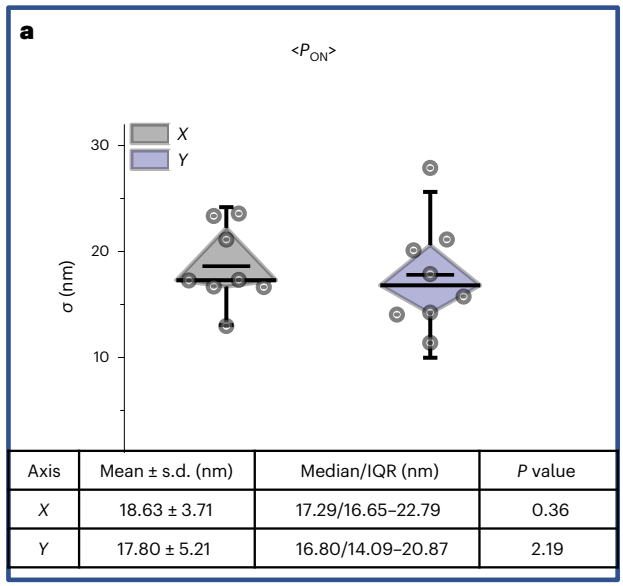

Axis	Mean ± s.d. (nm)	Median/IQR (nm)	*P* value
X	18.63 ± 3.71	17.29/16.65–22.79	0.36
Y	17.80 ± 5.21	16.80/14.09–20.87	2.19

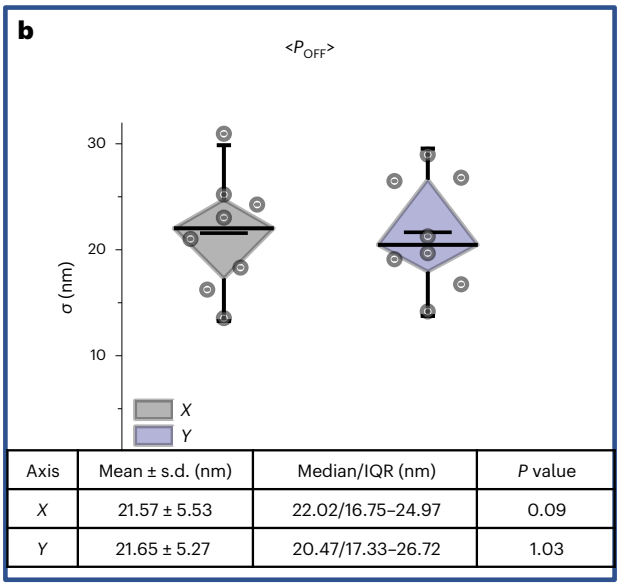

Axis	Mean ± s.d. (nm)	Median/IQR (nm)	*P* value
X	21.57 ± 5.53	22.02/16.75–24.97	0.09
Y	21.65 ± 5.27	20.47/17.33–26.72	1.03

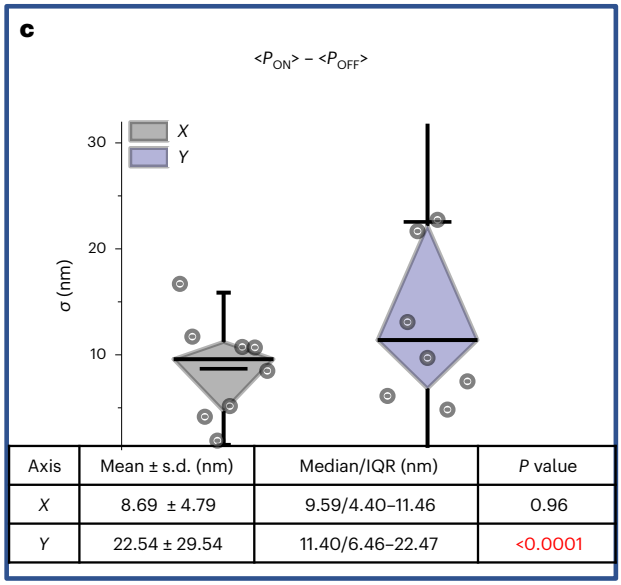

Axis	Mean ± s.d. (nm)	Median/IQR (nm)	*P* value
X	8.69 ± 4.79	9.59/4.40–11.46	0.96
Y	22.54 ± 29.54	11.40/6.46–22.47	<0.0001

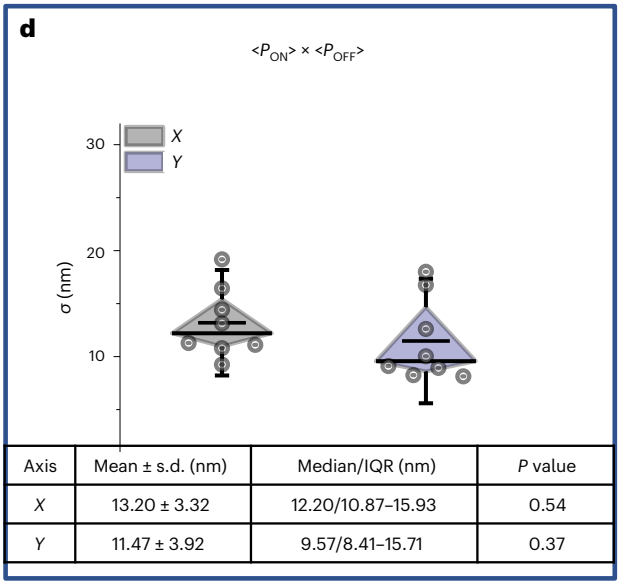

Axis	Mean ± s.d. (nm)	Median/IQR (nm)	*P* value
X	13.20 ± 3.32	12.20/10.87–15.93	0.54
Y	11.47 ± 3.92	9.57/8.41–15.71	0.37

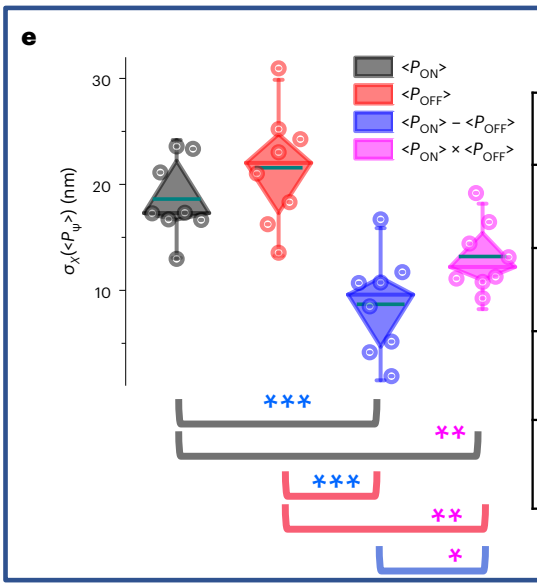

Comparison between conditions

	<P_{ON}>	<P_{OFF}>	<P_{ON}> – <P_{OFF}>
<P_{ON}>			
<P_{OFF}>	0.23 NS		
<P_{ON}> – <P_{OFF}>	0.0005 ***	0.0002 ***	
<P_{ON}> × <P_{OFF}>	0.0083 **	0.0034 **	0.0484 *

were obtained independently using a surface fit in two dimensions (2D) or by using an intensity variation in one dimension (1D) through the centres of detected events. The observed localization precision values $X_{2D}//Y_{2D}$ for the ON and OFF processes were 44.73 ± 1.26 nm/ /41.70 ± 1.78 nm and 38.83 ± 1.04 nm//38.47 ± 1.03 nm, respectively (Extended Data Fig. 5a,d). The $X_{1D}//Y_{1D}$ for the ON and OFF processes

https://doi.org/10.1038/s41565-022-01291-1

Fig. 4 | Comparison of standard deviations of the raw and processed error in fitting the centroid from ON and OFF processes. Representative scatter plots (circles) of eight isolated single particles below the limit of diffraction distributed in the field of view. **a**, Distribution of scatter plot and standard deviation along the *X* (grey) and *Y* (blue) directions for the PDF for the error in fitting the centroid of the ON process (<P_{ON}>). **b**, Distribution of scatter plot and standard deviation along the *X* (grey) and *Y* (blue) directions for the PDF for the error in fitting the centroid of the OFF process (<P_{OFF}>). **c**, Distribution of scatter plot and standard deviation along the *X* (grey) and *Y* (blue) directions for the PDF for the difference in error in functions of the ON and OFF processes (<$P_{ON} - P_{OFF}$>). **d**, Distribution of scatter plot and standard deviation along the *X* (grey) and *Y* (blue) directions for the PDF for the product in error in functions of the ON and OFF processes (<$P_{ON} \times P_{OFF}$>). **e**, Comparison of scatter plot and standard deviation of *X* axis (σ_x) of the PDF resulting from the fit of the error functions of <P_{ON}> (grey), <P_{OFF}> (red), <$P_{ON} - P_{OFF}$> (blue) and <$P_{ON} \times P_{OFF}$> (magenta). For all the distributions, the diagonal and the unconnected top and bottom edges of the diamond box indicate the median and interquartile range (IQR), while the smaller horizontal line (navy blue) parallel to the diagonal in the box and error bars indicates the mean and 10–90% of the data. All the distributions were tested using a D'Agostino and Pearson omnibus normality test. All distributions were normal except the *Y* axis of <$P_{ON} - P_{OFF}$>, which rejected the null hypothesis (in **c**, *P* value (red)). All data were thus analysed for mean ± standard deviation (s.d.) and median/IQR, presented below the corresponding distributions with the *P* value of the normality test conducted. The significance between the distributions shown in **e** was assessed using a two-tailed unpaired *t*-test with Welch's correction and is presented along with the *P* values in the table (right) adjacent to it; NS, not significant.

were found to be comparable to that of 2D and were measured to be 46.07 ± 4.37 nm//42.17 ± 1.61 nm and 41.53 ± 1.63 nm//40.62 ± 1.78 nm, respectively (Extended Data Fig. 5b,c,e,f). The localization precision of EM was also measured in a similar manner in 2D and 1D in the Hi state of the laser (Extended Data Fig. 6a). A comparison was also done for EM data for molecules that were simulated at a comparable SNR as that of the experimental data shown in Supplementary Table 2a (SNR, 20–30). In this case, the root mean square error values between the ground truth and localized fit based on the Nyquist criterion were calculated to be 9.90 ± 1.80 nm and 10.80 ± 1.80 nm in the principal and auxiliary axes, respectively (Extended Data Fig. 4b). The $X_{1D}//Y_{1D}$ for the same was comparable to that of 2D and was estimated to be 24.59 ± 0.88 nm//23.77 ± 0.70 nm (Extended Data Fig. 6b,c). Our results showed that in NM, the average standard deviation of error between the centroids of ON and OFF events of the same particle was 2.60 ± 0.81 nm with a full-width at half-maximum of 6 nm, better than the localization precision of single particles in EM.

EM detects only the high (Hi) state of the fluorescent particle, whereas NM records both ON and OFF events as nonlinear detections proportional to the rate of change of detected fluorescence intensities (Fig. 3a, ON, OFF). The fit of the intensity distribution of ON and OFF processes showed that these processes are diffraction limited (Extended Data Fig. 7a,b). The localization precision that is derived from the wavelet algorithm is the standard deviation in the probability density function (PDF) for the error in estimating the centre of emission of isolated single particles. The PDF values that we calculate for the ON and OFF processes (<P_{ON}> and <P_{OFF}>) encode the spatial information for the localization of the same molecule in a mutually exclusive manner (the ON versus OFF states of events) depending on the rate of change of intensity of the individual pixels (Fig. 3a, <P_{ON}> and <P_{OFF}>). We used this property to assess if the pointing accuracy could be improved by a linear combination (subtraction) or a nonlinear combination (multiplication) of PDFs (Fig. 3a, <$P_{ON} - P_{OFF}$> versus <$P_{ON} \times P_{OFF}$>, respectively). Subtraction and multiplication (<$P_{ON} - P_{OFF}$> and <$P_{ON} \times P_{OFF}$>) resulted in estimating the centroid with a better precision than <P_{ON}> or <P_{OFF}> (Figs. 3a and 4a–d). Though the median values of the localization precision estimated for <$P_{ON} - P_{OFF}$> and <$P_{ON} \times P_{OFF}$> were comparable, the interquartile range of <$P_{ON} - P_{OFF}$> for one axis displayed a higher spread than the interquartile range of the other axis, indicating an anisotropy in the PDF (Figs. 3a,b and 4c). We also failed to detect single particles due to the low SNR for the resulting function, derived as the difference of the PDFs between the ON and OFF processes. By contrast, the PDF derived by multiplication exhibited better isotropy, indicating that <$P_{ON} \times P_{OFF}$> is a more robust candidate to estimate the localization precision of subdiffracted particles (Fig. 3a,b and Extended Data Fig. 4d). The product PDF could be viewed as a joint distribution of the ON and OFF events, assuming them to be statistically independent. Interestingly, the localization precision values obtained from <$P_{ON} - P_{OFF}$> and <$P_{ON} \times P_{OFF}$> were approximately two times better when both ON and OFF processes were used than when only the ON process was used (Figs. 3b and 4e). Though the localization precision of NM was comparable to EM with almost no additional amplification factor, simple combinations of the error functions of the ON and OFF processes resulted in a significantly improved localization precision (Figs. 3b and 4e). The next generation of neuromorphic devices equipped with an on-chip amplification factor would improve the localization (~8–10 times better) of single particles with subnanometre precision (~8–10 times better).

Event detection allows better evaluation of fractalized diffusion

Since NM can record true events, we imaged freely diffusing fluorescent single particles (Fig. 5 and Extended Data Fig. 8). We detected freely diffusing beads in aqueous solution using EM at different sampling frequencies, namely, 50 Hz, 20 Hz and 10 Hz (Extended Data Fig. 8). When the integration time was 100 ms, the EM data showed differences in the median values of diffusion calculated from several trajectories, compared to 50 ms acquisition (Extended Data Fig. 8a–d). The 20 ms

Fig. 5 | Differential temporal binning of events from the neuromorphic camera allows insights into fractalized Brownian diffusion from individual trajectories. a, A gallery of five single particle trajectories from the same data reconstructed with different temporal samplings, namely, 10 Hz (100 ms), 20 Hz (50 ms), 40 Hz (25 ms), 50 Hz (20 ms) and 100 Hz (10 ms). Decreasing fractalization and an increase in the step size of the trajectories were observed as we decreased the sampling frequency from 100 Hz (10 ms, left) to 10 Hz (100 ms, right). Scale bar, 2.5 µm. **b**, Distribution of instantaneous diffusion coefficients (*D*) derived from the trajectories after the differential temporal accumulation of data obtained from NM (as shown in **a**), and their comparison to similar datasets acquired at 20 Hz (50 ms) using EM. The notch and boundaries of the box indicate the median and interquartile range, while the line (navy blue) in the box and error bars indicate mean and 10–90% of the data processed at different sampling rates in NM, and its comparison to the data acquired at 20 Hz (50 ms) using EM. One-way analysis of variance (ANOVA) followed by Fisher's least significant difference (LSD) test showed no notable differences between the presented datasets. **c**, Cumulative frequency distribution of log(*D*) of the trajectories obtained from the mobile trajectories post differential temporal binning in NM and its comparison to the data acquired at 20 Hz (50 ms) using EM. **d**, A plot of mean square displacement (MSD) versus time of the mobile trajectories after differential temporal binning in NM is compared to the data acquired at 20 Hz (50 ms) using EM. The mean square displacement is presented for the first ten points calculated from the mean of the mean square displacement values (circles) of all the detected trajectories. Error bars represent the s.e.m. Dotted lines represent the linear fit of each set of data. **e**, A zoomed-in plot of the area marked with a red dashed line in **d**, corresponding to sampling at high frequencies. The numbers of trajectories observed were 219 (10 ms), 150 (20 ms), 133 (25 ms), 86 (56 ms) and 53 (100 ms) for NM and 31 (50 ms) for EM.

https://doi.org/10.1038/s41565-022-01291-1

acquisition followed a smoother distribution compared to 50 ms and 100 ms but was not different (Extended Data Fig. 8b). The NM data were post processed at temporal windows of 10 ms, 20 ms, 25 ms, 50 ms and 100 ms. (Fig. 5a). Unlike EM, NM showed increased fractalization of diffusion with increased sampling frequencies (Fig. 5a). We compared the distribution of diffusion coefficients from NM to 50 ms data from EM and did not find a difference[31] (Fig. 5b and Supplementary Table 3). Additionally, the log-normalized curves also overlapped with each other (Fig. 5c and Supplementary Table 3). The average of the mean square displacement values from all trajectories showed that faster

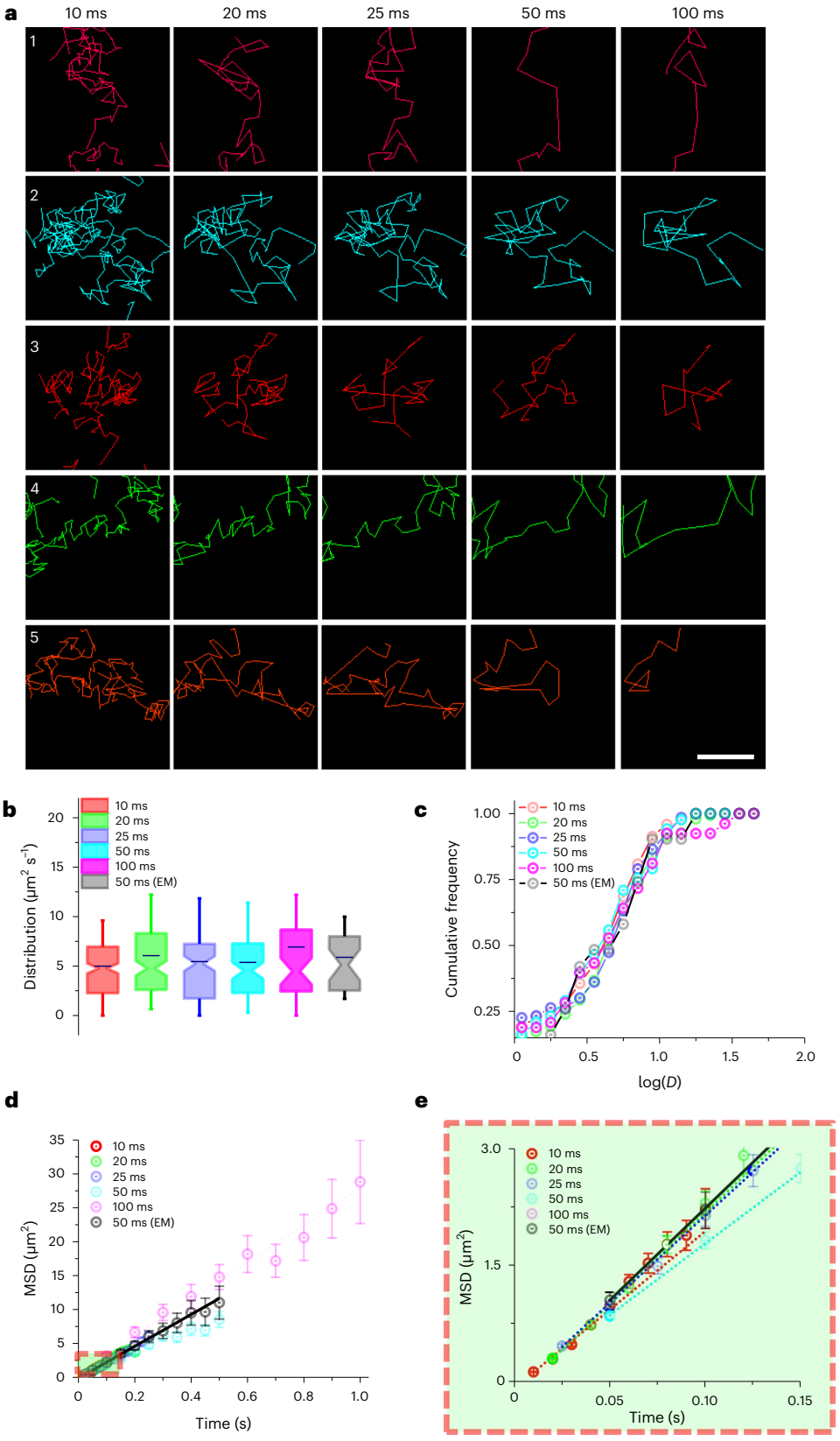

sampling resulted in a smaller step size and vice versa, but the slopes computed from the first ten points of the data were comparable (Fig. 5d,e and Supplementary Table 3). These observations demonstrate the advantage of NM over EM for studying fractalization of single particle trajectories; this advantage could be extended to study the sublinear, linear and super-linear nature of diffusion at various timescales. The diffusion characteristics were also not different between the ON and OFF processes when measured by NM detection (Extended Data Fig. 9a,b).

Single particle detection obtained from the OFF channel followed the same particle visualized in the ON channel when analysed through the DeepTrack algorithm (Extended Data Fig. 10a,b). The vectors starting from the centroids of ON events in one frame and going to the corresponding centroids of OFF events in the next frame were calculated as 'vector losses' between frames due to a slow accumulation rate (Extended Data Fig. 10c,d)[30]. The mean square displacements of two particles undergoing different types of Brownian motion ('confined' and 'diffuse') were calculated in the ON and the OFF channels separately for a period of 250 ms (Extended Data Fig. 10e,f). The frequency distribution of the step size of the 'diffuse' particle was right-shifted as compared to the 'confined' particle, consistent with the differences in the randomness of their movement (Extended Data Fig. 10g(i),(ii),h).

Conclusions

The ability of the neuromorphic camera to efficiently record transient events such as the disappearance of fluorescence makes it a powerful tool to surpass the diffraction limit, as we have shown, by combining the occurrence of ON/OFF events rather than analysing them separately. The localization precision (σ) of single fluorescent objects below diffraction limits relies on the number of photons (N) emitted per unit time ($\sigma \propto N^{-(1/2)}$)[4,5]. Such advances relying on nonlinear detection, as in NM, allow the localization of non-entangled events at a higher precision, allowing these measurements to achieve the super Heisenberg limit ($\sigma \propto N^{-(\Delta/2)}$, where $\Delta \geq 2$)[32,33]. Since neuromorphic cameras can record additional parameters in comparison to conventional photon integrating devices, event detection paradigms can be improved substantially by machine learning and artificial intelligence, reducing the digital footprint of the data needed for post processing and analysis. Advanced neuromorphic detectors could ameliorate the shortcomings of conventional imaging paradigms and open novel avenues in the detection of spatiotemporal processes.

Online content

Any methods, additional references, Nature Portfolio reporting summaries, source data, extended data, supplementary information, acknowledgements, peer review information; details of author contributions and competing interests; and statements of data and code availability are available at https://doi.org/10.1038/s41565-022-01291-1.

References

1. Nyquist, H. Certain topics in telegraph transmission theory. *Trans. Am. Inst. Electr. Eng.* **47**, 617–644 (1928).
2. Shannon, C. E. Communication in the presence of noise. *Proc. IRE* **37**, 10–21 (1949).
3. Betzig, E. Proposed method for molecular optical imaging. *Opt. Lett.* **20**, 237–239 (1995).
4. Betzig, E. et al. Imaging intracellular fluorescent proteins at nanometer resolution. *Science* **313**, 1642–1645 (2006).
5. Moerner, W. E. & Kador, L. Optical detection and spectroscopy of single molecules in a solid. *Phys. Rev. Lett.* **62**, 2535–2538 (1989).
6. Moerner, W. E. & Basché, T. Optical spectroscopy of single impurity molecules in solids. *Angew. Chem. Int. Ed.* **32**, 457–476 (1993).
7. Gahlmann, A. & Moerner, W. E. Exploring bacterial cell biology with single-molecule tracking and super-resolution imaging. *Nat. Rev. Microbiol.* **12**, 9–22 (2014).
8. Orrit, M. & Bernard, J. Single pentacene molecules detected by fluorescence excitation in a *p*-terphenyl crystal. *Phys. Rev. Lett.* **65**, 2716–2719 (1990).
9. Lacoste, T. D. et al. Ultrahigh-resolution multicolor colocalization of single fluorescent probes. *Proc. Natl Acad. Sci. USA* **97**, 9461–9466 (2000).
10. Thompson, R. E., Larson, D. R. & Webb, W. W. Precise nanometer localization analysis for individual fluorescent probes. *Biophys. J.* **82**, 2775–2783 (2002).
11. Shroff, H. et al. Dual-color superresolution imaging of genetically expressed probes within individual adhesion complexes. *Proc. Natl Acad. Sci. USA* **104**, 20308–20313 (2007).
12. Gallego, G. et al. Event-based vision: a survey. *IEEE Trans. Pattern Anal. Mach. Intell.* https://doi.org/10.1109/TPAMI.2020.3008413 (2020).
13. Posch, C. Bio-inspired vision. *J. Instrum.* **7**, C01054–C01054 (2012).
14. Miao, S. et al. Neuromorphic vision datasets for pedestrian detection, action recognition, and fall detection. *Front. Neurorobot.* **13**, 38 (2019).
15. Lichtsteiner, P., Posch, C. & Delbruck, T. A 128×128 120 dB 15 µs latency asynchronous temporal contrast vision sensor. *IEEE J. Solid-State Circuits* **43**, 566–576 (2008).
16. Son, B. et al. 4.1 A 640×480 dynamic vision sensor with a 9µm pixel and 300Meps address-event representation. In *Proc. 2017 IEEE International Solid-State Circuits Conference (ISSCC)* 66–67 (IEEE, 2017).
17. Liu, S. C. & Delbruck, T. Neuromorphic sensory systems. *Curr. Opin. Neurobiol.* **20**, 288–295 (2010).
18. Mead, C. Neuromorphic electronic systems. *Proc. IEEE* **78**, 1629–1636 (1990).
19. Mangalore, A. R., Seelamantula, C. S. & Thakur, C. S. Neuromorphic fringe projection profilometry. *IEEE Signal Process. Lett.* **27**, 1510–1514 (2020).
20. Liao, F., Zhou, F. & Chai, Y. Neuromorphic vision sensors: principle, progress and perspectives. *J. Semicond.* **42**, 013105 (2021).
21. Ham, D., Park, H., Hwang, S. & Kim, K. Neuromorphic electronics based on copying and pasting the brain. *Nat. Electron.* **4**, 635–644 (2021).
22. Hamilton, T. J., Afshar, S., Schaik, A. V. & Tapson, J. Stochastic electronics: a neuro-inspired design paradigm for integrated circuits. *Proc. IEEE* **102**, 843–859 (2014).
23. Lakshmi, A., Chakraborty, A. & Thakur, C. S. Neuromorphic vision: from sensors to event-based algorithms. *WIREs Data Min. Knowl. Discov.* **9**, e1310 (2019).
24. Kedia, S. et al. Real-time nanoscale organization of amyloid precursor protein. *Nanoscale* **12**, 8200–8215 (2020).
25. Nair, D. et al. Super-resolution imaging reveals that AMPA receptors inside synapses are dynamically organized in nanodomains regulated by PSD95. *J. Neurosci.* **33**, 13204–13224 (2013).
26. Mueggler, E., Rebecq, H., Gallego, G., Delbruck, T. & Scaramuzza, D. The event-camera dataset and simulator: event-based data for pose estimation, visual odometry, and SLAM. *Int. J. Robot. Res.* **36**, 142–149 (2017).
27. Annamalai, L., Chakraborty, A. & Thakur, C. S. EvAn: neuromorphic event-based sparse anomaly detection. *Front. Neurosci.* **15**, 699003 (2021).
28. Kechkar, A., Nair, D., Heilemann, M., Choquet, D. & Sibarita, J.-B. Real-time analysis and visualization for single-molecule based super-resolution microscopy. *PLoS One* **8**, e62918 (2013).
29. Izeddin, I. et al. Wavelet analysis for single molecule localization microscopy. *Opt. Express* **20**, 2081–2095 (2012).
30. Helgadottir, S., Argun, A. & Volpe, G. Digital video microscopy enhanced by deep learning. *Optica* **6**, 506–513 (2019).
31. Hedde, P. N. miniSPIM—a miniaturized light-sheet microscope. *ACS Sens.* **6**, 2654–2663 (2021).

32. Mitchell, M. W., Lundeen, J. S. & Steinberg, A. M. Super-resolving phase measurements with a multiphoton entangled state. *Nature* **429**, 161–164 (2004).
33. Napolitano, M. et al. Interaction-based quantum metrology showing scaling beyond the Heisenberg limit. *Nature* **471**, 486–489 (2011).

Methods

Preparation of fluorescent samples

TetraSpeck beads (0.1 µm, Thermo Fisher Scientific) were diluted to 1:10,000 of the stock solution. Some 200 µl of the solution was loaded in the chamber (Ludin Chamber, Life Imaging Services). To image the stationary molecules, the beads were immobilized on a precision cover-glass of thickness 170 ± 5 µm (no. 1.5H, Marienfeld). The rest of the medium was carefully exchanged with phosphate buffered saline (PBS) and loaded on to the microscope[24,25]. For single particle tracking experiments, the beads were imaged right after loading in the imaging chamber.

Microscopy configuration

Samples were imaged at 37 °C in an open chamber (Ludin Chamber, Life Imaging Services) mounted on an inverted motorized microscope (IX83, Olympus) equipped with a ×100, 1.49 numerical aperture objective allowing acquisition by total internal reflection fluorescence microscopy or oblique (highly inclined and laminated optical sheet) illumination to image stationary particles or for single particle tracking[24,25]. Samples were imaged using a 647 nm laser coupled to an acousto-optic tuneable filter (Roper Scientific). The acquisition was steered by MetaMorph software (Molecular Devices) in streaming mode at 50 ms, 75 ms and 100 ms, and the fluorescence was detected using a sensitive EMCCD camera (Delta Evolve, Photometric). The same set-up and conditions were used to image the samples with a neuromorphic camera (DAVIS 346, iniVation) using the Dynamic Vision Sensor (DVS) software. The samplings of the images in the EMCCD and neuromorphic camera in this configuration were 170 nm per pixel and 185 nm per pixel, respectively. The output data of NM was synchronized with EM to temporally align images with a frame rate equal to the switching period of the lasers to mimic the EM acquisition rate when required. The acquisition of the EMCCD was synchronized to either continuous illumination of the lasers or to a defined switching period using MetaMorph software.

Image reconstruction

NM records event streams as (t,x,y,p), where t is the time stamp, x and y are the coordinates of the pixels and p is the polarity of the event[14]. Continuously acquired data is saved as a stream of asynchronous events (*.aedat4 file type)[14,23]. The temporal resolution of the camera is in the range of a few microseconds. The events are accumulated into frames by visualizing the ON events (pseudo-coloured in green) and OFF events (pseudo-coloured in red) in user-specified temporal windows (such as 50 or 100 ms). The code also allows one to create frames of unequal integration time periods[26]. A fluorescence emission event from a particle is recorded as an event denoting 'positive polarity' or 'negative polarity' at those individual pixels. A positive polarity is recorded if there is an increase in intensity relative to the previous time stamp, while a decrease in intensity is recorded as a 'negative polarity' event. The events corresponding to positive polarity are referred to as ON events, while negative polarity events are referred to as OFF events. When there is no intensity fluctuation, there are no measurements. The maximum speed of acquisition was around 10^6 frames s^{-1} (1 polarity μs^{-1}). The polarity changes have a latency of around 20 µs (ref. 12). The frame rate can be chosen by the user post acquisition and allows one to study ensemble or single particle fluorescence with a wide range of temporal resolutions.

Temporal sampling

The events sampled by NM are stored as an *.aedat4 file type. These events are visualized using an accumulator algorithm that integrates the event polarities in specified time intervals. To reduce the latency, the pixel integration time must be more than 20 µs per frame[26]. The events were accumulated into images of defined intervals to generate a stack of Portable Network Graphics (*.png) images to analyse the spatial and temporal variability of signals. The images were split into red, green and blue (RGB) channels on ImageJ, and the mean intensity of a region containing a single TetraSpeck bead was measured throughout the stack for ON (green) and OFF (red) events independently. This determines the individual positive and negative polarities for a single fluorescent bead over time. The difference in the mean pixel intensities of the ON events and OFF events results in a net change in polarity and determines the temporal increase or decrease in intensity. The net polarities were then cumulatively summed over time to display the true integrated intensity with time. The polarity, integrated polarity and integrated intensity thus generated were further analysed temporally. The pixel intensities of the OFF events were plotted on the negative axis to represent negative polarity.

NM detection of single fluorescent particles between the Hi and Lo states was repeated for switching periods of 100 ms, 75 ms and 50 ms (Supplementary Table 1a). Asynchronous data from NM was integrated at 5 ms per frame to carry out temporal analysis. The FFT of the temporal fluctuations in intensity was used to determine the switching period of the single fluorescent particle, and a Gaussian curve fit on the FFT determined the standard deviation of the period of switching of the single particle fluorescence (Supplementary Table 1a). Additionally, the FFT revealed that the ON and OFF events were almost completely out of phase. A small overlap of 0.1π radian of the ON and OFF events was observed at the beginning of each cycle. FFTs of both the integrated polarity (Supplementary Table 1b) and the integrated intensity (Supplementary Table 1c) confirmed the switching period of the fluorescent particle to be in resonance with the laser.

Estimation of dynamic range

The data obtained from EM or NM were converted to 16-bit Tagged Image File Format (*.tif) image streams encoded with the information for spatial and temporal sampling. For the temporal sampling of data from EM, the rate of image acquisition was defined by the integration time for a single frame set at the time of imaging. For NM, the temporal sampling was obtained by post processing the raw data, where the integration time was defined for single frames to generate image stacks. The dynamic range was calculated by finding the maximum signal recorded by the beads for the EM and NM data. The aforesaid values were converted to a $\log_2$ scale for analysis and for plotting the dynamic range of the detectors in each experimental condition. For calculation of the SNR of EM, isolated fluorescent particles were detected in 15×15 pixel^2 boxes. The data were converted to a ratio of maxima by minima of the corresponding boxes. For the NM data, a similar analysis was performed by calculating the ratio of maxima of the detected single particle within a box size of 15×15 pixel^2 to the maxima of a random region, which did not record any fluorescent single particles. MetaMorph was used for region measurements.

Wavelet segmentation for localization and particle tracking

For immobilized fluorescent beads, NM detection of single fluorescent particles between Hi and Lo was repeated for a switching period of 100 ms, 75 ms and 50 ms and reconstructed with the frame rate equal to the switching frequency between high and low illumination intensities. For evaluating mobility, several particles displaying Brownian motion were imaged using NM. The recorded NM data were reconstructed as images with accumulation frequencies of 10 Hz, 20 Hz, 40 Hz, 50 Hz and 100 Hz (corresponding to 100 ms, 50 ms, 25 ms, 20 ms and 10 ms per frame, respectively). For EM, the data were acquired at sampling frequencies of 10 Hz, 20 Hz and 50 Hz (corresponding to 100 ms, 50 ms and 20 ms, respectively). Since the wavelet-based approach provided better segmentation, we initially used it to localize and track the particles. The data obtained from EM and NM were converted to a *.tif stream (16 bit) encoded with the spatial and temporal sampling, as explained previously. Single molecule localization microscopy data generated were analysed to extract the single particle position and

dynamics. Single fluorescent particles were localized in each image frame and tracked over time by the wavelet segmentation algorithm and simulated annealing, respectively[28,29,34]. The software package used to derive quantitative data on protein localization and dynamics was run as a plug-in within the MetaMorph software environment. Under these experimental conditions, the localization precision for single molecules in direct stochastic optical reconstruction microscopy was between 19 ± 3.3 nm for Alexa Fluor 647 dye, as quantified from 2D intensity distributions of 25 isolated single molecules[24,25]. Localization of molecules was performed by choosing 75% of the auto thresholding from PalmTracer, a plug-in supported by MetaMorph[25]. For tracking, we chose trajectories containing a minimum length of two consecutive time points with a maximum distance travelled of less than 50 μm s^{-1}, and a maximum blinking interval of 1 second to reconnect the trajectories. The error in fitting the single molecules was reconstructed as an image using PalmTracer. Each experimentally driven probability function obtained was identified and quantified using PalmTracer. Probability density functions were quantified using a 2D Gaussian fitting, from which the principal (σ_x) and the auxiliary (σ_y) axes were determined. The fitting was performed on each molecule or event in EM and NM, respectively.

Particle localization using deep learning

The Keras and TensorFlow framework-based deep learning algorithm DeepTrack (Python 3.7) was used for tracking of single fluorescent particles[30]. The convolutional neural network returns the x and y coordinates of the centroids of particles and the distance (r) of the predicted centroid (x, y) from the centre of each frame[30]. The neural network architecture was used as provided[30]. It consists of three convolutional layers, the first of which results in 16 feature maps of size 49 × 49 $pixels^2$, which is down-sampled to 24 × 24 by a maximum-pooling (max-pooling) layer; the second layer results in 32 feature maps of size 22 × 22 $pixels^2$, which is further down-sampled to 11 × 11 by max-pooling; and the final convolutional layer results in 64 feature maps of size 9 × 9 $pixels^2$, which is down-sampled to 4 × 4 by a max-pooling layer. The outputs of the final max-pool layer are then fed to two dense top layers that perform a regression to determine the x and y coordinates and the distance r from the centre of the frame. The CNNs were trained on a simulated dataset of about 1.5 million images using the DeepTrack image generation function[30]. The image generation routine uses the Bessel function as the point spread function for simulating images of the particles (Extended Data Fig. 4 and Supplementary Table 4). The algorithm allowed us to generate simulated particles with different intensities, Airy discs, SNR values and intensity gradients that are chosen randomly from a uniform distribution within user-defined constraints. The neural networks were trained on successive batches of 5,000, 4,000, 2,500, 1,000 and 500 containing 8, 32, 128, 512 and 1,024 simulated images, respectively[35]. Each simulated image contained between one and four particles in each frame, with the ground truth defined as the centroid of the particle closest to the centre of the frame. The parameter values used to generate these images to simulate single particles for NM and EM data can be found in Supplementary Table 4. Each input frame was rescaled to 51 × 51 $pixels^2$ by DeepTrack, and an overlapping 'scanning box' then scanned each frame for particles. The distribution of centroid predictions for particles was chosen only if it was smaller than a user-defined threshold corresponding to the full-width at half-maxima of the Gaussian of the wide-field detection[30] (Supplementary Table 5). When a single particle is detected in multiple scanning boxes, the different predictions were attributed to a single particle based on an inter-centroid distance threshold. The average of the centroid predictions from all the scanning boxes was taken as the centroid for the particle[30].

Training and tracking using DeepTrack algorithm

The neural networks were trained by generating simulated images as indicated in the DeepTrack repository[30]. DeepTrack allows fine tuning of the parameters of simulated particles to closely match the particles detected by EM and NM. The predictions can be optimized by tuning multiple parameters, as explained in Supplementary Table 4. The size of the scanning boxes and the distance between the subsequent scanning boxes used for predictions of both EM and NM data are provided in Supplementary Table 5. The particle radial distance threshold allows one to select only those predictions that are smaller than the given threshold values for analysing the localization precision. Additionally, in instances where a single particle is detected by multiple scanning boxes in the same frame, an inter-centroid distance threshold allowed us to allocate the predictions to that single particle. Once trained, the CNN was tested using simulated images of particles in different uniform ranges of SNRs (25 particles for each range of SNRs), and the localization precision was calculated in each case. The results are shown in Extended Data Fig. 4.

Spatial sampling

The events were reconstructed to images by integrating at a frame rate equal to the laser switching period. Some 200 image frames were created for stationary single fluorescent beads that display continuous emission. The stack of images was split into ON (green) and OFF (red) events and converted to video (*.avi) format using ImageJ. The CNN was trained to track centroids of single particles in the two videos independently. The x and y coordinates of the centroids were extracted as Excel files using customized macros developed in Python.

Estimation of localization precision

The localization precision of the independent particles was detected by two methods. First, we extracted the surface distribution of error in the mean of every detected particle. The error in calculating the centroid or localization precision was estimated as the standard deviation of the 2D surface Gaussian fit along the x (major/principal) and y (minor/auxilliary) axes. The localization precision thus obtained is denoted as X_{2D} and Y_{2D}. In the second method, we identified the principal and auxiliary axes of the detected single particles and fit a 1D Gaussian. The frequency distribution of the error in the mean was plotted independently. The standard deviation obtained from the independent Gaussian fit was also used as a measure of localization precision. The localization precision thus obtained is denoted as X_{1D} and Y_{1D}.

Single particle tracking using DeepTrack algorithm

The NM frames were split into ON and OFF events using ImageJ. The ON (new position of the particle) and OFF (initial position of the particle) events were tracked using DeepTrack and analysed independently at 100 Hz to compare with the wavelet method. The mean square displacements of the two particles ('confined' and 'diffuse') were calculated in the green and red channels separately for a period of 250 ms and the results were displayed using Origin (v.2015, Origin Labs)[24,25]. The step sizes between time points for the two particles were calculated and a frequency distribution was obtained. The displacements between the centroid of ON events in one frame and the centroid of OFF events in the subsequent frame of a single particle were shown as vectors whose direction is given from green to red. The cumulative frequency of the step sizes of both the particles was also plotted in Origin. Correlation plots between ON and OFF events were generated in Origin.

Statistics

Statistical analysis and significances were performed using GraphPad Prism v.7.04 for Windows, GraphPad Software (www.graphpad.com). The D'Agostino–Pearson omnibus normality test and Shapiro–Wilk normality test were used to test the normal distribution. All statistical values are shown as mean ± s.e.m. for normally distributed data or as median (interquartile range, 25% to 75% interval) for non-normally distributed data, unless otherwise indicated. Normally distributed datasets were compared using a two-tailed unpaired Student's t-test

(for two group); a one-way ANOVA test followed by Tukey's multiple comparison test and Fisher's LSD test (for multi-group); or a Welch's correction (for one group). Non-normally distributed datasets were tested by a non-parametric two-tailed Mann–Whitney test (for two group). The surface maps for the X and Y intensity datasets and all graphs were plotted using Origin v.2015, Sr2, 69.2.272, Origin Lab (https://www.originlab.com), unless otherwise stated. Significance is indicated by $^{*}P \leq 0.05$, $^{**}P \leq 0.01$ and $^{***}P \leq 0.001$; NS, $P > 0.05$.

Visual demonstration of data analysis pipeline

The schematic representation for imaging and spatiotemporal analysis of single fluorescent particles was created with BioRender under paid subscription (Extended Data Fig. 1). The analysis pipeline used for acquisition and analysis of the localization of ON and OFF events recorded from diffraction-limited objects is demonstrated in Supplementary Video 1. The objects were localized with nanoscale precision, and single particle trajectories at millisecond timescales were generated.

Reporting summary

Further information on research design is available in the Nature Portfolio Reporting Summary linked to this article.

Data availability

An example dataset of neuromorphic events, the reconstructed frames and instructions for use are available for download on Github: https://github.com/neuromorphicmicroscopy/Neuromorphic-Localisation-Microscopy. The rest of the data that support the findings of this study are available as Supplementary Information. Source data are provided with this paper.

Code availability

The work presented here used codes that were already available.

The version of the code used for extraction of data from the neuromorphic camera is available from D.N. and C.S.T. on request. Codes that are central to the conclusions and inferences made in the manuscript regarding the reconstruction of frames, pipelines built using DeepTrack and instructions for use are available for download on Github: https://github.com/neuromorphicmicroscopy/Neuromorphic-Localisation-Microscopy.

PalmTracer is an all-in-one software package for the analysis of single molecule localization microscopy data that can be downloaded from https://neuro-intramuros.u-bordeaux.fr/displayresearchprojects/70/11.

The instructions and codes required for synchronizing the neuromorphic camera with other devices are available on Github: https://inivation.gitlab.io/dv/dv-docs/docs/external-camera-sync/ and https://github.com/uzh-rpg/rpg_dvs_ros.

References

34. Racine, V. et al. Multiple-target tracking of 3D fluorescent objects based on simulated annealing. In *Proc. 3rd IEEE International Symposium on Biomedical Imaging: From Nano to Macro* 1020–1023 (IEEE, 2006).
35. Smith, S. L., Kindermans, P.-J. & Le, Q. V. Don't decay the learning rate, increase the batch size. In *Proc. 6th International Conference on Learning Representations* (OpenReview, 2018); https://openreview.net/forum?id=B1Yy1BxCZ

Acknowledgements

We thank all the members of the Nanoorg lab at the Centre for Neuroscience, Indian Institute of Science (IISc) for helpful discussions and comments. We also thank L. Annamalai, V. Ramanathan (C.S.T.'s lab) and A. Adiga (C.S.S.'s lab) for their help and suggestions during the early stages of the project. We thank J.B. Sibarita at the Interdisciplinary Institute for Neuroscience, Bordeaux for sharing the analysis paradigms for single molecule localization and tracking. We also thank B. Jayaprakash, S. P. Arun and S. Devarajan at the Centre for Neuroscience, IISc for helpful discussions. A major part of this work was generously supported by grants from the IISc under the Institute of Eminence (IISc-IOE) programme to C.S.S., C.S.T. and D.N. It was also supported by the Department of Biotechnology (Innovative Young Biotechnologist Award to D.N. and M.J.); Department of Biotechnology Genomics Engineering Taskforce to D.N.; Department of Biotechnology (DBT) Ramalingaswami Fellowship to D.N. and M.J.; DBT–IISc partnership programme to D.N.; IISC-STAR programme grant to D.N.; Science and Engineering Research Board (Early Career Research Award to M.J.); University Grants Commission, India to D.N.; and Tata Trusts, India for the programme grant (co-investigator, D.N.). N.S. thanks the CSIR Senior Research Associateship/Scientists Pool Scheme. C.S.S. and C.S.T. also thank the Pratiksha Trust for their support to procure the neuromorphic cameras. D.N. sincerely thanks colleagues at the Division of Biological Science, IISc for allowing access to older/discarded microscopes either in full or in part for research and development.

Author contributions

D.N., C.S.S. and C.S.T. conceived the idea. R.M. and D.N. designed the research; R.M. and/or D.N. performed all the experiments unless otherwise indicated; R.M., N.S. and D.N. performed the analysis; N.S. and M.J. prepared the samples; and C.S.T. and C.S.S. shared neuromorphic devices and analytical tools to optimize and extract information from the neuromorphic camera. R.M., M.J. and D.N. wrote the manuscript. All the authors read, provided critical input on and approved the final version of the manuscript.

Competing interests

The authors declare no competing interests.

Additional information

Extended data is available for this paper at https://doi.org/10.1038/s41565-022-01291-1.

Supplementary information The online version contains supplementary material available at https://doi.org/10.1038/s41565-022-01291-1.

Correspondence and requests for materials should be addressed to Deepak Nair.

Peer review information *Nature Nanotechnology* thanks Boxin Shi, Giovanni Volpe and the other, anonymous, reviewer(s) for their contribution to the peer review of this work.

https://doi.org/10.1038/s41565-022-01291-1

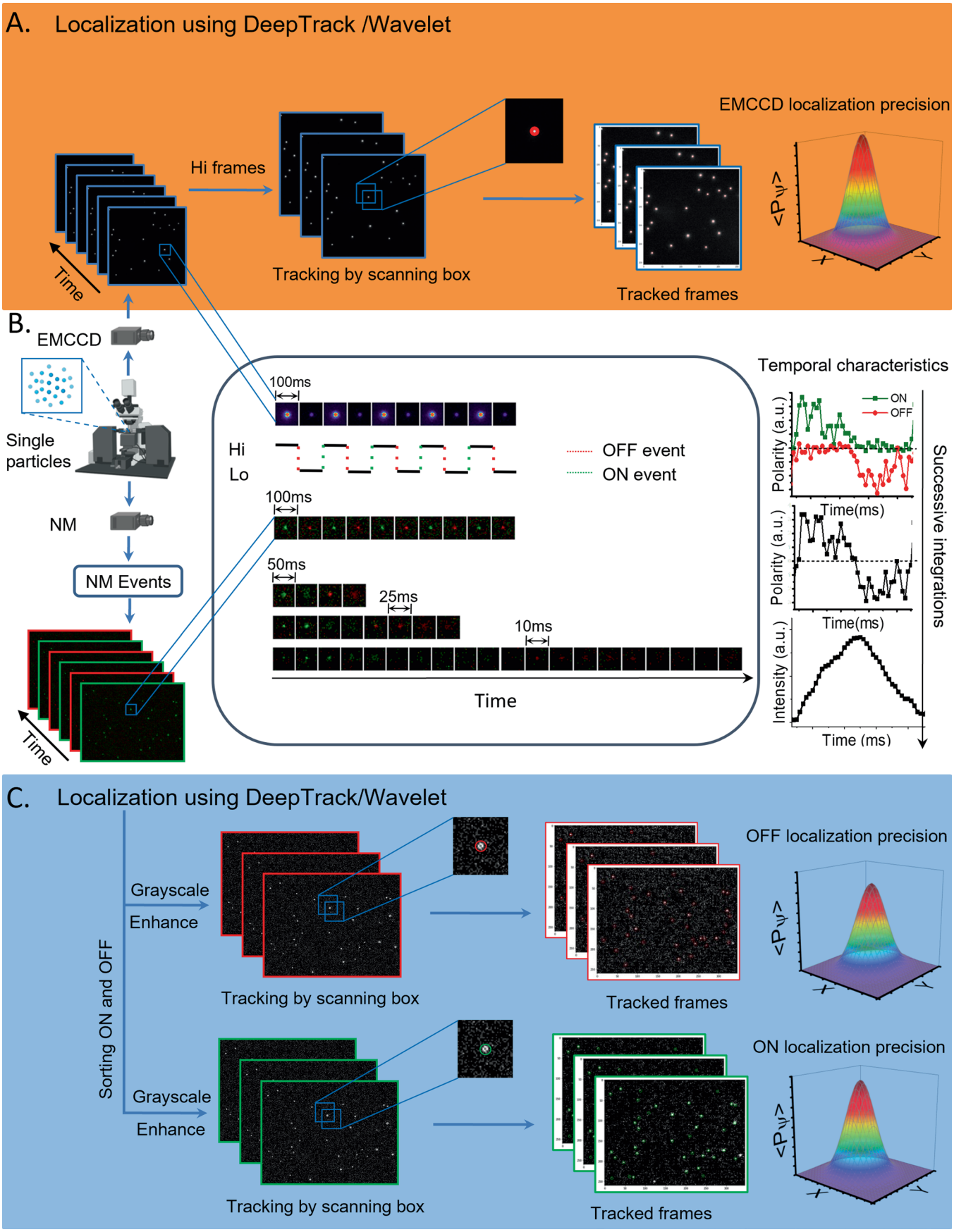

Extended Data Fig. 1 | See next page for caption.

https://doi.org/10.1038/s41565-022-01291-1

Extended Data Fig. 1 | Scheme for imaging and spatiotemporal analysis of single fluorescent particles. a) Spatial localization of single fluorescent particles imaged at 10 Hz using an EMCCD camera (EM) using either DeepTrack or a wavelet algorithm. Only frames in which the laser was at Hi intensity were chosen for particle tracking, unless otherwise stated. The frames in which the laser was at Lo intensity were discarded due to low visibility of particles. A scanning box shifts through each frame predicting the centroids of particles (marked with red circles). A 2D frequency distribution fit was used to determine the Gaussian profile of localization. **b**) Temporal dynamics of a single fluorescent particle. The laser was periodically pulsed between Hi and Lo periods of 100 ms each. The pseudo-coloured intensity map of a single fluorescent particle as imaged by EM shows that alternate frames have high and low intensity fluorescence, corresponding to the laser intensity. The asynchronous data from the NM camera (NM) was accumulated at frame rates of 10 Hz, 20 Hz, 40 Hz, and 100 Hz with positive polarity (ON) in green and negative polarity (OFF) in red. Asynchronous data from NM was accumulated at 200 Hz, and the ON (green) and OFF (red) channels were analyzed separately to study the temporal characteristics of fluorescence. The ON and OFF polarities were summed to study the temporal characteristics of total change in polarity. The accumulated polarity was further integrated in time, which provided the total intensity of the particle. **c**) Spatial localization of single fluorescent particles imaged using NM. The asynchronous data was accumulated at 10 Hz. Frames with a rising edge of laser intensity show ON events of particles (green). The frames with a falling edge show OFF events of particles (red). The frames with ON (green box) and OFF events (red box) were sorted. A scanning box shifts through each frame predicting the centroids of particles (marked with red and green circles in OFF and ON frames, respectively). A 2D distribution fit determined the Gaussian profile of localization for ON and OFF events separately. Figure created with BioRender.com.

https://doi.org/10.1038/s41565-022-01291-1

A.

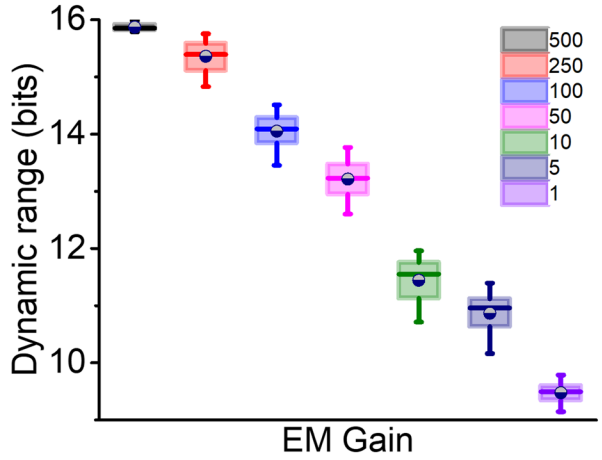

EM

Condition (EM gain)	Median	IQR
500	15.85	15.82-15.92
250	15.39	15.11-15.59
100	14.09	13.84-14.29
50	13.23	12.93-13.47
10	11.55	11.04-11.55
5	10.96	10.57-10.96
1	9.50	9.34-9.60

B.

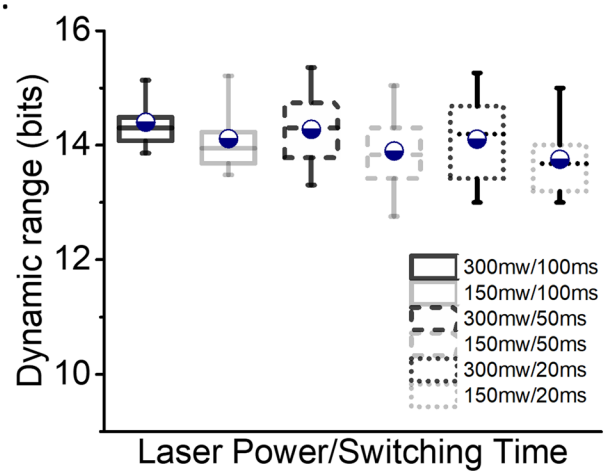

NM

Condition (Only ON)	Median	IQR	N
300mW/100ms	14.30	14.07-14.49	970
300mW/50ms	14.30	13.78-14.74	860
300mW/20ms	14.19	13.41-14.68	527
150mW/100ms	13.94	13.68-14.22	859
150mW/50ms	13.83	13.41-14.30	860
150mW/20ms	13.68	13.19-14.00	1326

C.

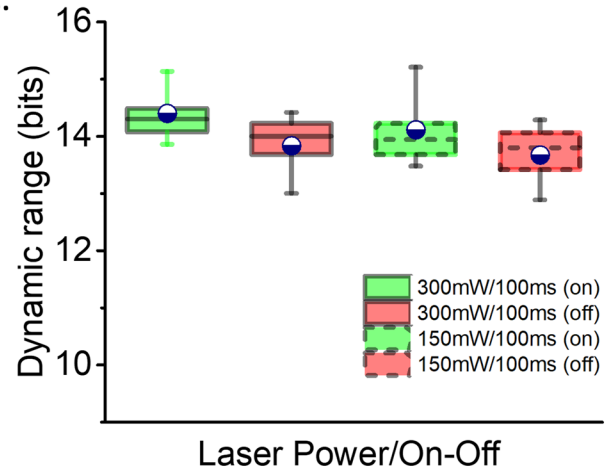

NM

Condition ON/OFF	Median	IQR
300mW/100ms ON	14.30	14.07-14.49
300mW/100ms OFF	14.00	13.68-14.22
150mW/100ms ON	13.94	13.68-14.22
150mW/100ms OFF	13.80	13.41-14.06

Extended Data Fig. 2 | See next page for caption.

https://doi.org/10.1038/s41565-022-01291-1

Extended Data Fig. 2 | Comparison of the dynamic range of EM and NM. a) Progressive increase in the bit depth was observed as we increased the electron multiplying gain of the EM obtained from 400 localized single particles. **b**) The response of the NM at the same laser intensity (300 mW) that captures maximum dynamic range for EM (16 bit). There were no differences in the bit depth when the switching time changed between 20 ms, 50 ms or 100 ms for the ON process in the NM, but the bit depth was decreased with laser power. NM data was acquired in the same illumination conditions where the EM recorded the signals with the highest dynamic range (300 mW output laser power, 28-29 mW at the objective). While on the EM, recording was performed at 10 Hz (100 ms), NM was exposed to increased switching frequency for ON and OFF processes, as well as to high (similar to EM conditions) and low laser powers (150 mW output laser power, 15-16 mW at the objective). N indicates the number of localized ON events from isolated single particles. **c**) No difference was found in the dynamic range between ON and OFF processes (970 ON/OFF events at 300 mW and 990 (ON) and 980 (OFF) events at 150 mW) of the NM, indicating that both processes were detected with the same efficiency of detection. For all the distributions, the inner horizontal line and boundaries of the box indicate median and interquartile range (IQR), while the diameter (separating navy blue/white circle) in the box and error bars on the box indicate mean and 10-90 % of the data. All the distributions were non-normal by D'Agostino and Pearson Omnibus normality test (for all data $p < 0.0001$) and thus analyzed for median and interquartile range (IQR), as presented towards the right side of their corresponding distributions.

https://doi.org/10.1038/s41565-022-01291-1

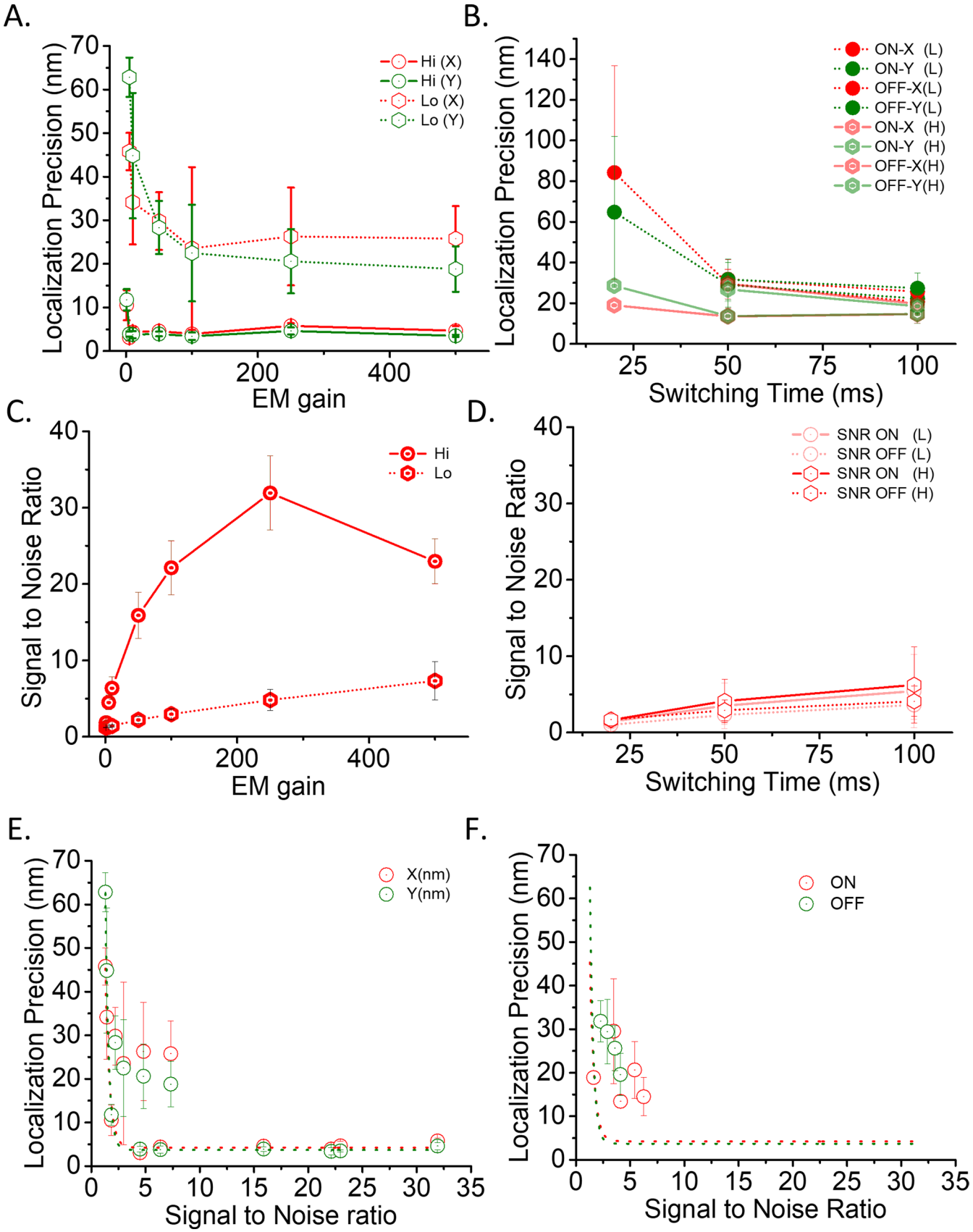

Extended Data Fig. 3 | See next page for caption.

https://doi.org/10.1038/s41565-022-01291-1

Extended Data Fig. 3 | Comparison of localization precision and signal to noise ratio between EM and NM. To examine the dependence of centroid estimation on SNR in an EM, we calculated the localization precision and SNR at various EM gain by taking the ratio of maximum to minimum signal detected in a 15×15 pixel^2 compartment around the pixel displaying maximum intensity. **a**) Localization precision in X (red) and Y (green) directions for Hi (circle and solid line) and Lo (pentagon and dotted line) laser powers on the EM, respectively. The variance in error for calculating the centroid of the single fluorescent particle increased with a decrease in EM gain. **b**) Localization precision in X (red) and Y (green) directions for ON and OFF processes of NM data at ON (pentagon and solid line) and OFF (circle and solid line) states. The variance of localizing centroid increased with decrease in laser power. **c**) Signal to noise ratio (SNR) of the EM at different EM gain for Hi (circle and solid line) and Lo (pentagon and dotted line) illumination. **d**) Signal to noise ratio of the NM at different switching powers for ON (solid line) and OFF (dotted line) processes. The recording was done with ON (pentagon) and OFF (circle) laser powers. **e**) A plot of signal to noise ratio vs localization precision in EM in the X (red circle) and Y (green circle) directions. Dotted red and green line indicate the sigmoidal fit of the data. An increase in signal to noise ratio decreased the variance of detecting the centroid and increased the accuracy of detection. **f**) A plot of signal to noise ratio vs localization precision in NM for X axis for ON (red circle) and OFF (green circle) processes. Dotted red and green lines indicate the sigmoidal fit for the same in EM. All error bars indicate SD. All EM analysis was performed on 4 molecules. For NM data at 300 mW, 10 and 5 single particles were analyzed for ON process, whereas 9 and 6 particles were detected for OFF process at 100 ms and 50 ms switching time. At 150 mW, 13, 6 and 8 single particles were analyzed for ON process, while 13, 3 and 9 particles were detected for OFF processes at 100 ms, 50 ms and 20 ms switching time.

https://doi.org/10.1038/s41565-022-01291-1

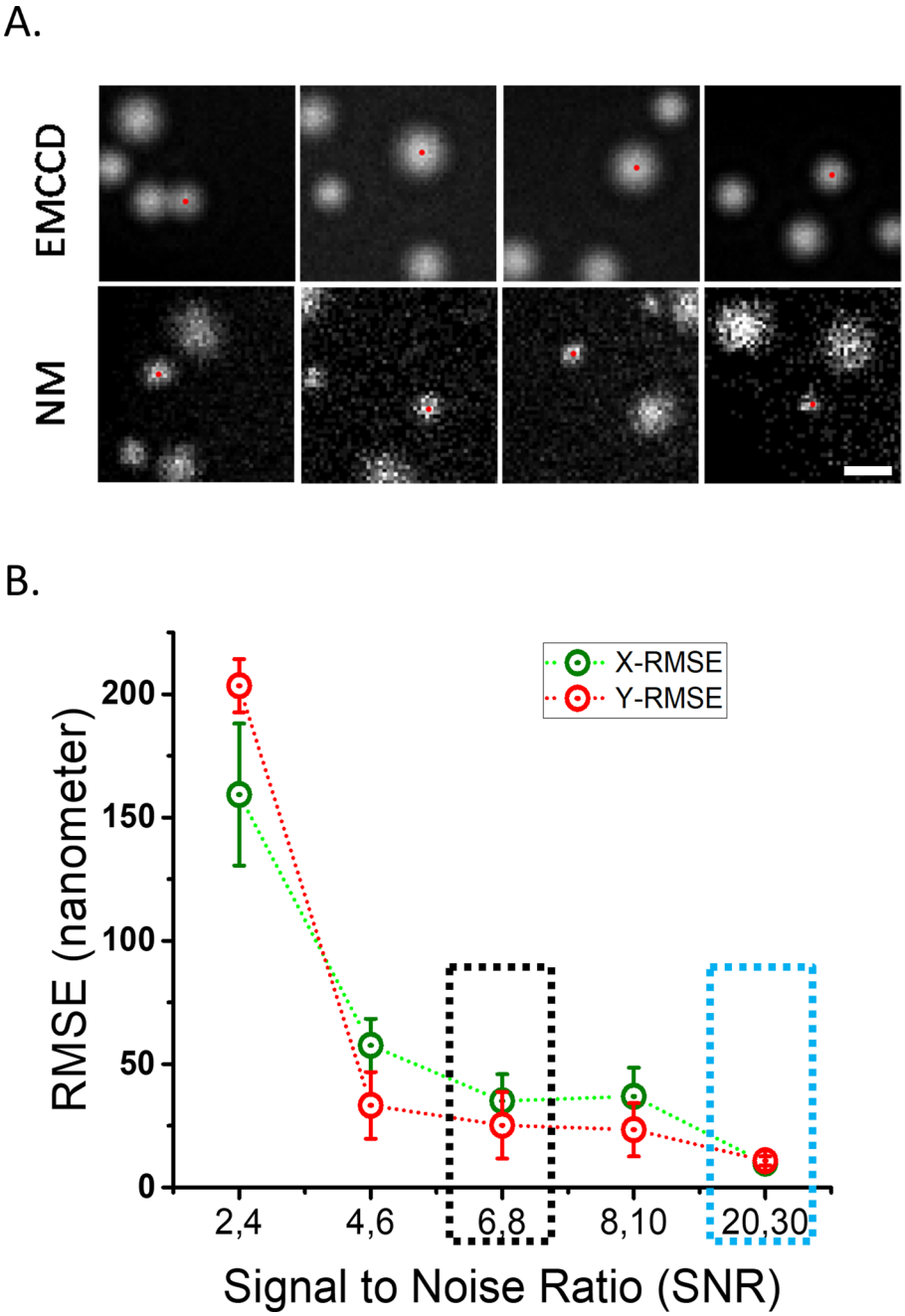

Extended Data Fig. 4 | Gallery of sample images of EM (top) and NM (bottom) as generated for training of the CNN. a) The images were generated using the algorithm provided by DeepTrack and training parameters were optimized. The red dots indicate the ground truth centroid coordinated for training the CNN. Each individual panel is 244 × 244 pixel ^{2}. Scale bar indicates 61 pixels. **b**) The root mean square error in predicting the centroid of the simulated single particles was calculated with respect to the ground truth for each range of SNR and the average root mean square error (data point) and SEM (error bars) for X (green) and Y (red) directions were plotted when sampled at Nyquist rate. X axis indicates the lower and upper range of simulation for SNR for the simulated particles. Black and blue dotted regions indicate the experimental ranges of SNR obtained for immobilized fluorescent particles using NM and EM under similar experimental conditions. 25 images were simulated for each range of SNR, a trained CNN was used to predict the centroid of the particle and the root mean square was calculated for each range of SNR.

https://doi.org/10.1038/s41565-022-01291-1

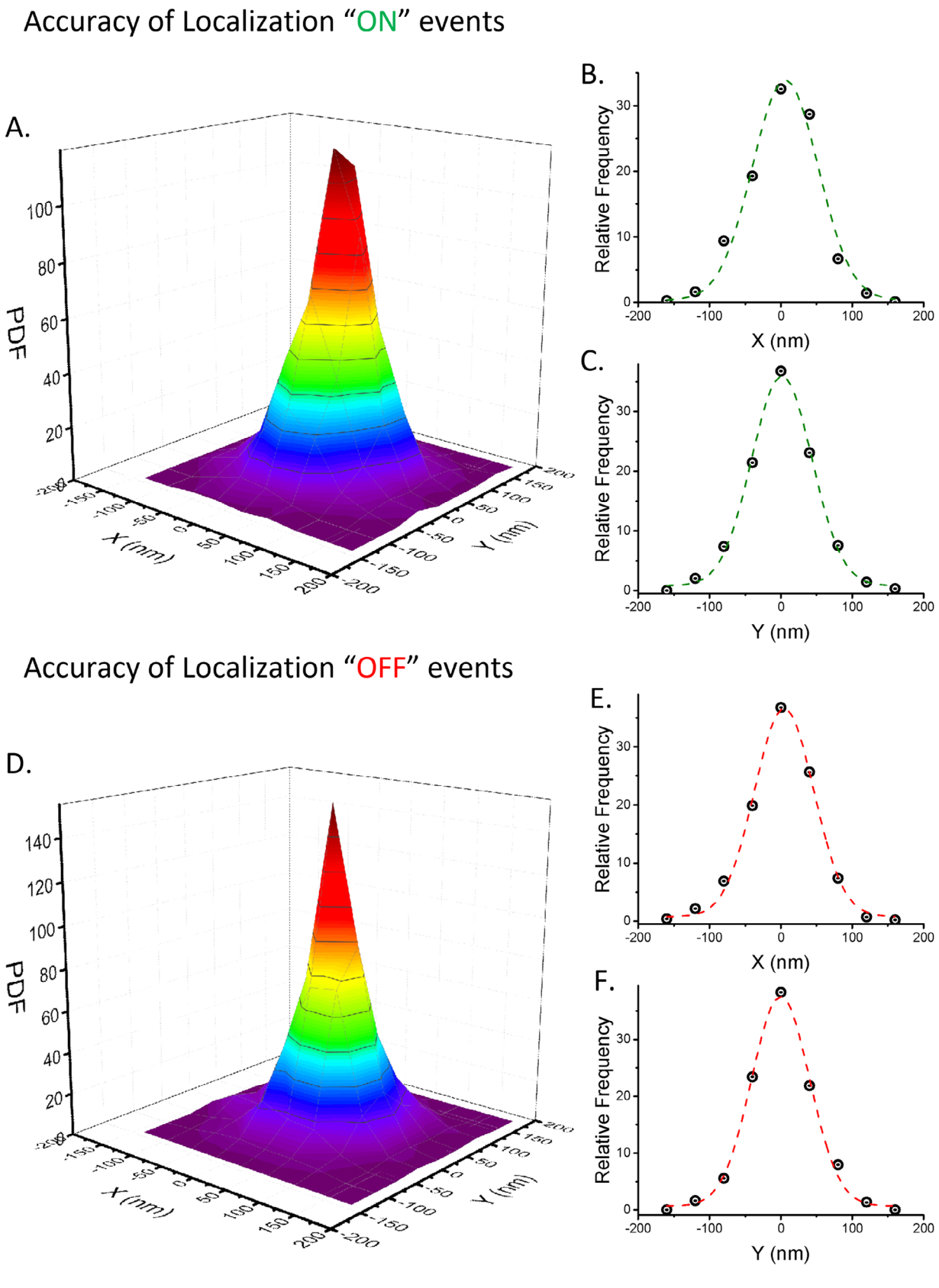

Extended Data Fig. 5 | See next page for caption.

https://doi.org/10.1038/s41565-022-01291-1

Extended Data Fig. 5 | Normalized localization precision of isolated and immobilized sub diffraction sized single fluorescent particles using neuromorphic imaging. a) Probability density function (p.d.f.) of centroids (normalized to (0,0)) as obtained by DeepTrack for ON events of 15 fluorescent beads over 100 frames accumulated at 100 ms. A 2D Gaussian surface fit determined X_{2D} and Y_{2D} to be 44.73 + /−1.26 nm and 41.70 + /−1.17 nm, respectively. **b**) Relative frequency distribution (data points) of normalized X and Y coordinates during ON events obtained by DeepTrack for 15 fluorescent beads over 100 frames. A Gaussian amplitude fit (green dotted line) determined X_{1D} to be 46.07 + /−4.37 nm. **c**) A Gaussian amplitude fitting (green dotted line) determined Y_{1D} to be 42.17 + /−1.61 nm. **d**) P.d.f. of centroids (normalized to (0,0)) obtained by DeepTrack for OFF events of 15 fluorescent beads over 100 frames accumulated at 100 ms. A 2D Gaussian surface fit estimated X_{2D} and Y_{2D} to be 38.83 + /−1.04 nm and 38.47 + /−1.03 nm, respectively. **e**) Relative frequency distribution (data points) of normalized x and y coordinates during ON events as obtained by DeepTrack for 15 fluorescent beads over 100 frames. A Gaussian amplitude fit (red dotted line) determined X_{1D} to be 41.53 + /−1.63 nm. F) A Gaussian amplitude fit (green dotted line) determined Y_{1D} to be 40.62 + /−1.78 nm. Centroid estimation in 1D and 2D is presented as mean + /− standard deviation.

https://doi.org/10.1038/s41565-022-01291-1

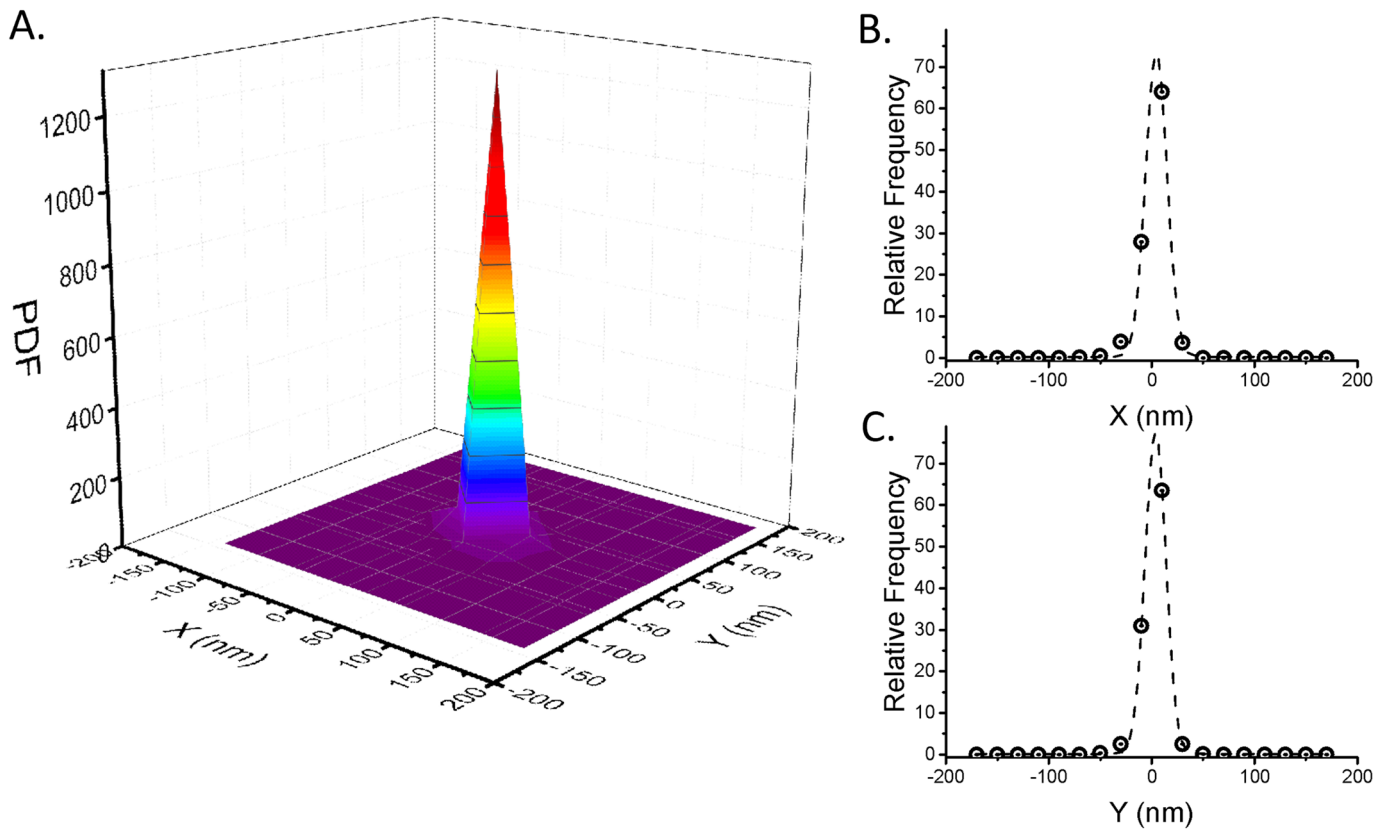

Extended Data Fig. 6 | Normalized localization precision of isolated and immobilized sub-diffraction sized single fluorescent particles using EM. **a**) P.d.f. of centroids (normalized to (0,0)) obtained by DeepTrack for Hi images from EM of 15 fluorescent beads over 100 frames accumulated at 100 ms. A 2D Gaussian surface fit determined X_{2D} and Y_{2D} to be 15.24 + /−0.11 nm and 14.08 + /−0.15 nm, respectively. **b**) Relative frequency distribution (data points) of normalized x and y coordinates during ON events obtained by DeepTrack for 15 fluorescent beads over 100 frames. A Gaussian amplitude fit (black dotted line) determined X_{1D} to be 24.59 + /−0.88 nm. **c**) A Gaussian amplitude fit (black dotted line) determined Y_{1D} to be 23.77 + /−0.70 nm. Centroid estimation in 1D and 2D is presented as mean ± standard deviation.

https://doi.org/10.1038/s41565-022-01291-1

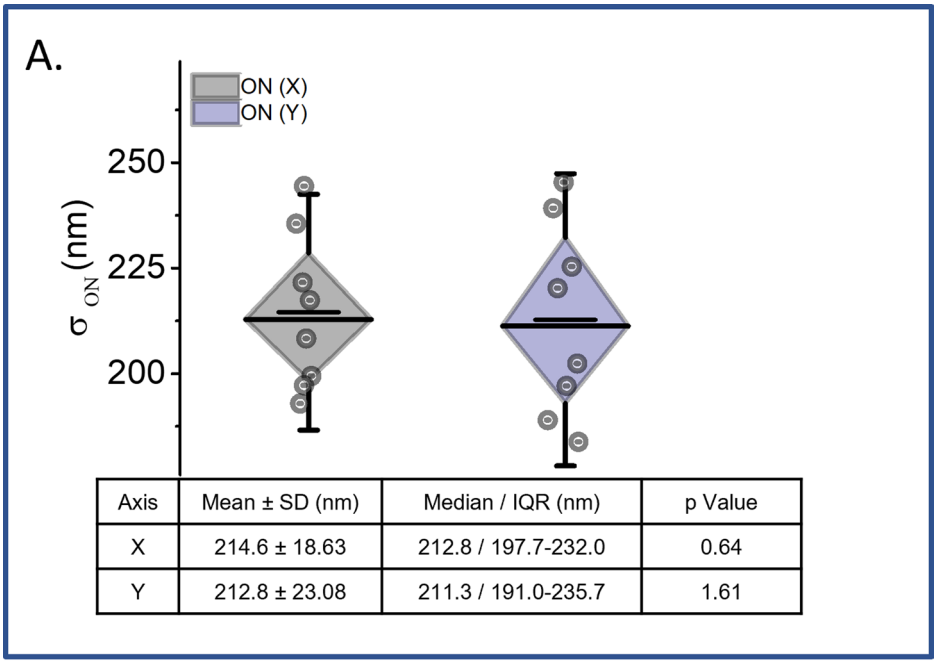

Axis	Mean ± SD (nm)	Median / IQR (nm)	p Value
X	214.6 ± 18.63	212.8 / 197.7-232.0	0.64
Y	212.8 ± 23.08	211.3 / 191.0-235.7	1.61

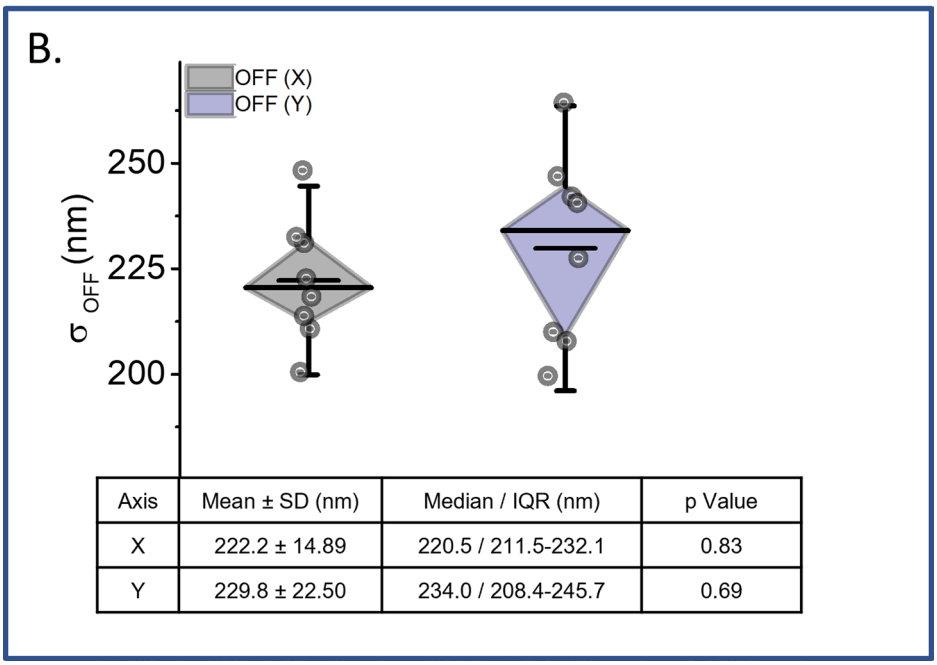

Axis	Mean ± SD (nm)	Median / IQR (nm)	p Value
X	222.2 ± 14.89	220.5 / 211.5-232.1	0.83
Y	229.8 ± 22.50	234.0 / 208.4-245.7	0.69

Extended Data Fig. 7 | Comparison of standard deviation for the ON and OFF processes as detected by NM. Representative scatter plots (circles) of eight isolated single particles below the limit of diffraction distributed in the field of view. **a**) Distribution of standard deviation along X (grey) and Y (blue) directions for diffraction limited fluorescence emission from ON processes of neuromorphic detection. **b**) Distribution of standard deviation along X (grey) and Y (blue) directions for diffraction limited fluorescence emission from OFF processes of neuromorphic detection. For all the distributions, the diagonal and the unconnected top and bottom edges of the diamond box indicate median and IQR, while the smaller horizontal line (navy blue) parallel to the diagonal in the box and error bars indicate mean and 10–90 % of the data. All the distributions passed D'Agostino and Pearson omnibus normality test. All data were thus analyzed for mean + /− standard deviation (SD) and median / interquartile range (IQR) is presented below the corresponding distributions with the p value of the normality test conducted.

https://doi.org/10.1038/s41565-022-01291-1

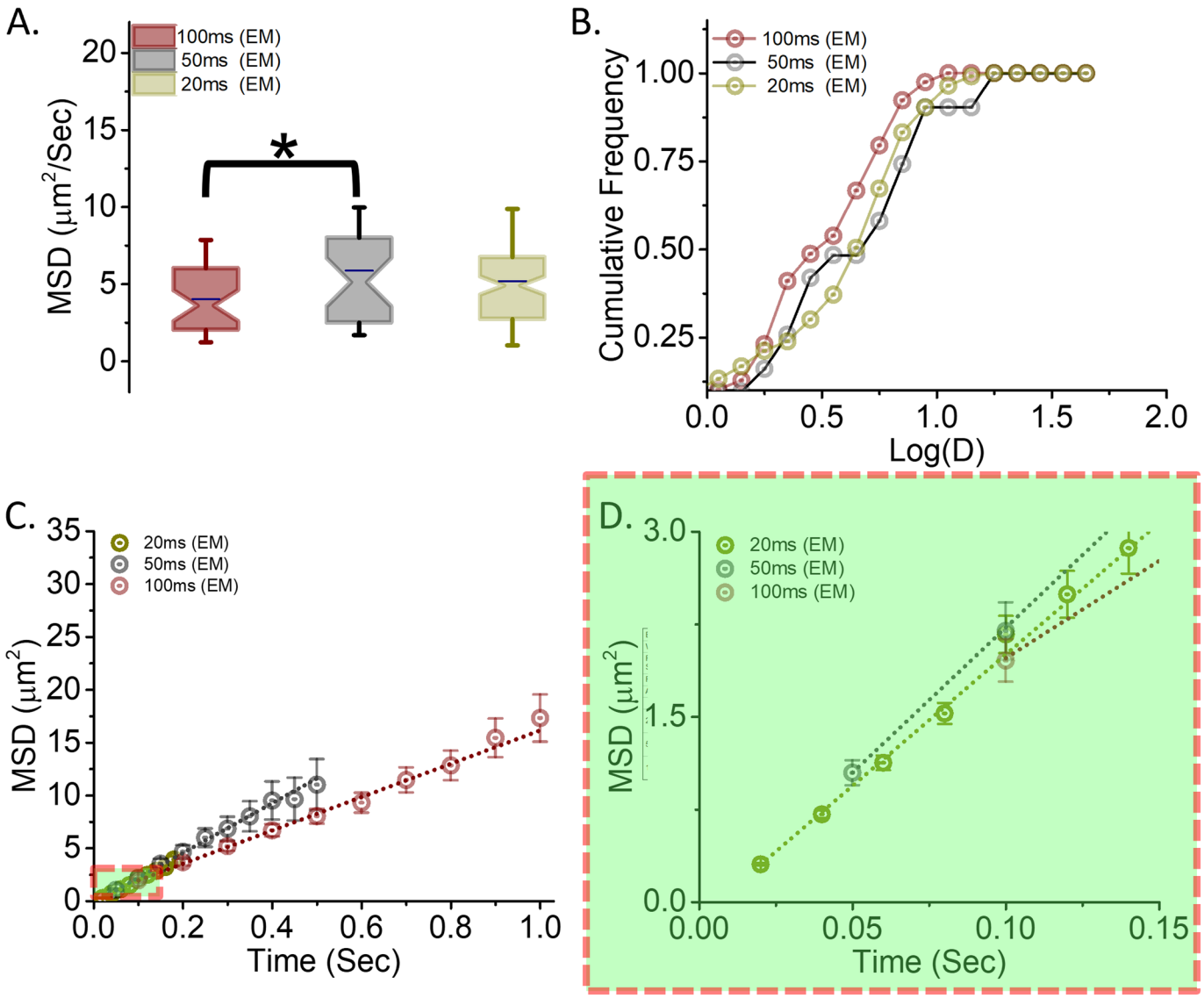

Extended Data Fig. 8 | Differential evaluation of temporal sampling of diffusion from EM. a) Distribution of instantaneous diffusion coefficients derived from the trajectories after differential temporal sampling of data from EM. The notch and boundaries of the box indicate median and IQR, while the line (navy blue) in the box and error bars display mean and 10-90 % of the data. The data acquired at 10 Hz (100 ms), 20 Hz (50 ms) and 50 Hz (20 ms), as colour coded in wine, grey and yellow, respectively were compared. The distribution of data obtained at 10 Hz (100 ms) was significantly different from that at 20 Hz (50 ms) (p value = 0.0293), as assessed by One-way Anova followed by Fisher's LSD test, in contrast to 50 Hz (20 ms) which remained similar. **b**) Cumulative frequency distribution of log(*D*) of the mobile trajectories for different temporal sampling using EM. The distribution of data obtained at 10 Hz (100 ms) was shifted towards lower values when compared to 20 Hz (50 ms), while 50 Hz (20 ms) remained similar. **c**) A plot of mean square displacement vs time of the mobile trajectories for differential temporal sampling using EM. The MSD is presented for the first 10 points calculated from the mean of the MSDs of all the detected trajectories. Error bar represents the standard error of the mean (SEM). **d**) The plot represents the zoomed version of the red inset marked in **c**, corresponding to sampling at very high frequencies. The number of trajectories observed were 39, 31 and 113 for 100 ms, 50 ms and 20 ms, respectively.

https://doi.org/10.1038/s41565-022-01291-1

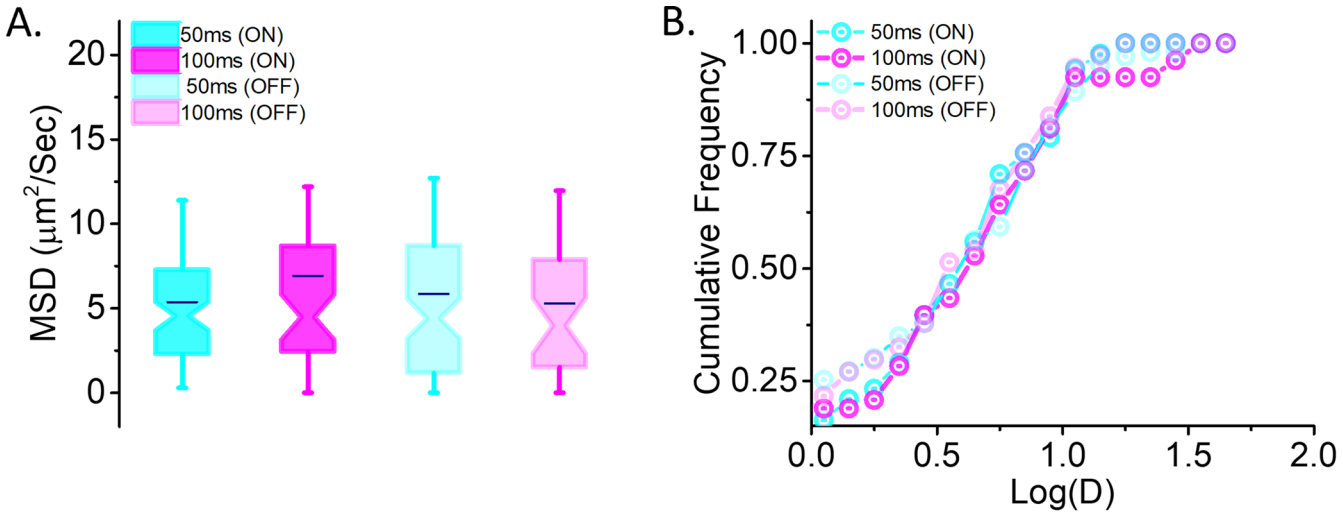

Extended Data Fig. 9 | Analysis of trajectories obtained from ON and OFF events from NM are not different. a) Distribution of instantaneous diffusion coefficient derived from the trajectories of ON and OFF processes after differential temporal sampling of 10 Hz and 20 Hz (corresponding to 100 ms and 50 ms, respectively). The notch and boundaries of the box indicate median and IQR, while the line (navy blue) in the box and error bars indicate mean and 10-90 % of the data. No significant differences using One-way Anova followed by Fisher's LSD test were reported between ON and OFF process at 10 Hz (dark and light magenta) and 20 Hz (dark and light cyan). **b**. Cumulative frequency distribution of log(*D*) of the mobile trajectories of ON and OFF processes at 10 Hz (dark and light magenta) and 20 Hz (dark and light cyan). The number of trajectories observed were 86 (50 ms, ON), 53 (100 ms, ON), 103 (50 ms, OFF) and 37 (100 ms, OFF).

https://doi.org/10.1038/s41565-022-01291-1

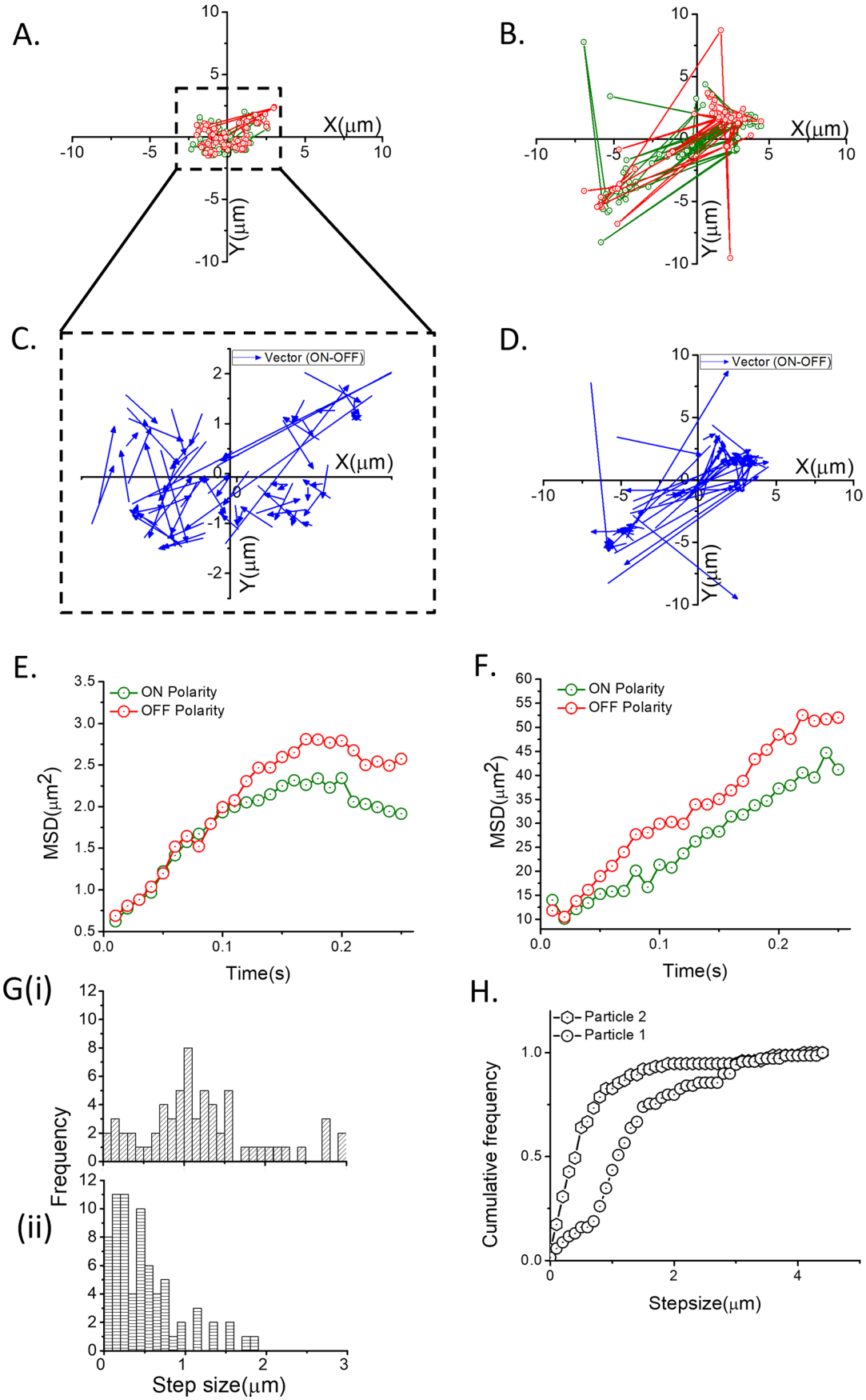

Extended Data Fig. 10 | See next page for caption.

https://doi.org/10.1038/s41565-022-01291-1

Extended Data Fig. 10 | Event based detection of single fluorescent particle trajectories using neuromorphic imaging. a) Normalized trajectories of ON (green) and OFF (red) events of a confined particle (particle 1). A single fluorescent particle was tracked using NM and the corresponding asynchronous data generated was accumulated at 10 ms per frame for 100 frames. The frames were split into RGB channels and the DeepTrack neural network was used to track the position of the particles in the green (ON events signifying new position of particle in that frame) and red (OFF events signifying the initial position of the particle in that frame) channels separately. **a, b**) Normalized trajectories of ON events (green) and OFF events (red) of a confined (Particle 1) and diffuse particle (particle 2). **c, d**) Vector loss between consecutive frames. Vectors pointing from the centroids of ON events in one frame to the corresponding centroids of OFF events in the subsequent frame for confined and diffuse particles. **e, f**) Mean square displacement (MSD) of confined and diffuse particles. The MSD was calculated for the ON (green) and OFF (red) events independently using their respective trajectories. The MSDs of the two channels showed high correlation. **g**) Frequency distribution of step sizes of single fluorescent particle trajectories. The step size of an isolated particle was calculated as the distance between centroids of OFF and ON events in one frame to those in the subsequent frame. The step sizes of both particles were distributed into bin sizes of 100 nm. The distribution of step sizes for particle 2 (G(i)) was right shifted (showing a higher number of larger steps) as compared to particle 1(G(ii)), which was more confined. **h**) Cumulative frequency distribution of step sizes of particles 1 (circle) and 2 (hexagon). The diffused particle had a larger slope than the confined one due to larger step size.

nature portfolio

Corresponding author(s): DEEPAK NAIR

Last updated by author(s): Oct 20, 2022

Reporting Summary

Nature Portfolio wishes to improve the reproducibility of the work that we publish. This form provides structure for consistency and transparency in reporting. For further information on Nature Portfolio policies, see our Editorial Policies and the Editorial Policy Checklist.

Statistics

For all statistical analyses, confirm that the following items are present in the figure legend, table legend, main text, or Methods section.

n/a	Confirmed
☐	☒ The exact sample size (*n*) for each experimental group/condition, given as a discrete number and unit of measurement
☐	☒ A statement on whether measurements were taken from distinct samples or whether the same sample was measured repeatedly
☐	☒ The statistical test(s) used AND whether they are one- or two-sided *Only common tests should be described solely by name; describe more complex techniques in the Methods section.*
☒	☐ A description of all covariates tested
☐	☒ A description of any assumptions or corrections, such as tests of normality and adjustment for multiple comparisons
☐	☒ A full description of the statistical parameters including central tendency (e.g. means) or other basic estimates (e.g. regression coefficient) AND variation (e.g. standard deviation) or associated estimates of uncertainty (e.g. confidence intervals)
☒	☐ For null hypothesis testing, the test statistic (e.g. *F*, *t*, *r*) with confidence intervals, effect sizes, degrees of freedom and *P* value noted *Give P values as exact values whenever suitable.*
☒	☐ For Bayesian analysis, information on the choice of priors and Markov chain Monte Carlo settings
☒	☐ For hierarchical and complex designs, identification of the appropriate level for tests and full reporting of outcomes
☒	☐ Estimates of effect sizes (e.g. Cohen's *d*, Pearson's *r*), indicating how they were calculated

Our web collection on statistics for biologists contains articles on many of the points above.

Software and code

Policy information about availability of computer code

Data collection

Samples were imaged on an inverted motorized microscope (allowing acquisition by TIRF or oblique (Highly inclined and Laminated Optical Sheet) illumination to image stationary particles or for single particle tracking . Samples were imaged using a 647 nm laser coupled to an acousto-optic tuneable filter (Roper Scientific, France). The acquisition was steered by MetaMorph software (Molecular Devices) in streaming mode at 50 ms, 75 ms and at 100 ms and the fluorescence was detected using a sensitive EMCCD camera (Delta Evolve, Photometric). The same setup and conditions were used to image the samples with a neuromorphic camera (DAVIS 346, iniVation) using the Dynamic Vision Sensor (DVS) Software. The sampling of the images in EMCCD and neuromorphic camera in this configuration were 170 nm/pixel and 185 nm/pixel, respectively.

Data analysis

The analysis of the acquired data was performed in MetaMorph software (7.10.1.181), Origin 2015, Sr2, 69.2.272, and GraphPad PRISM (8.4.2).
Wavelet Segmentation for localization and particle tracking: The algorithm for quantitative data analysis of protein localization was performed using PALM-TRACER (PALMTRACERX64, 2017) plugin in MetaMorph software.
Particle localization and tracking using deep learning-The Keras and TensorFlow framework based deep learning algorithm, DeepTrack, was used for tracking of single fluorescent particles. The algorithms were developed and optimized on Python 3.7
The surface maps for X, Y intensity data sets and all graphs were plotted using Origin 2015, Sr2, 69.2.272, Origin lab, USA nd GraphPad PRISM (8.4.2).
D'Agostino-Pearson Omnibus normality test and Shapiro-Wilk normality test were used to test normal distribution.
Normally distributed datasets were compared using two-tailed unpaired Student's t-test (for two- group) or one-way analysis of variance (ANOVA) test followed by Tukey's multiple comparison test (for multi-group). Non-normally distributed datasets were tested by non-parametric two-tailed Mann-Whitney test (for two-group).
Schemes were made using Biorender and Videos were made as Windows power point presentation and then converted in to Video using the

customize video option on powerpoint

For manuscripts utilizing custom algorithms or software that are central to the research but not yet described in published literature, software must be made available to editors and reviewers. We strongly encourage code deposition in a community repository (e.g. GitHub). See the Nature Portfolio guidelines for submitting code & software for further information.

Data

Policy information about availability of data

All manuscripts must include a data availability statement. This statement should provide the following information, where applicable:

- Accession codes, unique identifiers, or web links for publicly available datasets
- A description of any restrictions on data availability
- For clinical datasets or third party data, please ensure that the statement adheres to our policy

Data Availability Statement
Example dataset of neuromorphic events, the reconstructed frames, and instructions for use are available for download on Github - https://github.com/neuromorphicmicroscopy/Neuromorphic-Localisation-Microscopy. Rest of the data that support the findings of this study are available from the corresponding author (DN) upon reasonable request.

Code availability statement
The presented work utilized already available codes.

The version of the code used for extraction of data from Neuromorphic Camera is available from DN and CST on request. Codes that are central to the conclusions and inferences made in the manuscript regarding reconstruction of frames, pipelines built using DeepTrack, and instructions for use are available for download on Github - https://github.com/neuromorphicmicroscopy/Neuromorphic-Localisation-Microscopy.

PALMTracer is an all-in-one software package for the analysis of Single Molecule Localization Microscopy (SMLM) data which can be downloaded from https://neuro-intramuros.u-bordeaux.fr/displayresearchprojects/70/11

The instructions and codes required for synchronizing Neuromorphic Camera with other devices is available on Github - https://inivation.gitlab.io/dv/dv-docs/docs/external-camera-sync/ and https://github.com/uzh-rpg/rpg_dvs_ros

Human research participants

Policy information about studies involving human research participants and Sex and Gender in Research.

Reporting on sex and gender	*Use the terms sex (biological attribute) and gender (shaped by social and cultural circumstances) carefully in order to avoid confusing both terms. Indicate if findings apply to only one sex or gender; describe whether sex and gender were considered in study design whether sex and/or gender was determined based on self-reporting or assigned and methods used. Provide in the source data disaggregated sex and gender data where this information has been collected, and consent has been obtained for sharing of individual-level data; provide overall numbers in this Reporting Summary. Please state if this information has not been collected. Report sex- and gender-based analyses where performed, justify reasons for lack of sex- and gender-based analysis.*
Population characteristics	*Describe the covariate-relevant population characteristics of the human research participants (e.g. age, genotypic information, past and current diagnosis and treatment categories). If you filled out the behavioural & social sciences study design questions and have nothing to add here, write "See above."*
Recruitment	*Describe how participants were recruited. Outline any potential self-selection bias or other biases that may be present and how these are likely to impact results.*
Ethics oversight	*Identify the organization(s) that approved the study protocol.*

Note that full information on the approval of the study protocol must also be provided in the manuscript.

Field-specific reporting

Please select the one below that is the best fit for your research. If you are not sure, read the appropriate sections before making your selection.

☐ Life sciences ☐ Behavioural & social sciences ☐ Ecological, evolutionary & environmental sciences

For a reference copy of the document with all sections, see nature.com/documents/nr-reporting-summary-flat.pdf

Life sciences study design

All studies must disclose on these points even when the disclosure is negative.

Sample size	*Describe how sample size was determined, detailing any statistical methods used to predetermine sample size OR if no sample-size calculation was performed, describe how sample sizes were chosen and provide a rationale for why these sample sizes are sufficient.*
Data exclusions	*Describe any data exclusions. If no data were excluded from the analyses, state so OR if data were excluded, describe the exclusions and the rationale behind them, indicating whether exclusion criteria were pre-established.*
Replication	*Describe the measures taken to verify the reproducibility of the experimental findings. If all attempts at replication were successful, confirm this OR if there are any findings that were not replicated or cannot be reproduced, note this and describe why.*
Randomization	*Describe how samples/organisms/participants were allocated into experimental groups. If allocation was not random, describe how covariates were controlled OR if this is not relevant to your study, explain why.*
Blinding	*Describe whether the investigators were blinded to group allocation during data collection and/or analysis. If blinding was not possible, describe why OR explain why blinding was not relevant to your study.*

Behavioural & social sciences study design

All studies must disclose on these points even when the disclosure is negative.

Study description	*Briefly describe the study type including whether data are quantitative, qualitative, or mixed-methods (e.g. qualitative cross-sectional, quantitative experimental, mixed-methods case study).*
Research sample	*State the research sample (e.g. Harvard university undergraduates, villagers in rural India) and provide relevant demographic information (e.g. age, sex) and indicate whether the sample is representative. Provide a rationale for the study sample chosen. For studies involving existing datasets, please describe the dataset and source.*
Sampling strategy	*Describe the sampling procedure (e.g. random, snowball, stratified, convenience). Describe the statistical methods that were used to predetermine sample size OR if no sample-size calculation was performed, describe how sample sizes were chosen and provide a rationale for why these sample sizes are sufficient. For qualitative data, please indicate whether data saturation was considered, and what criteria were used to decide that no further sampling was needed.*
Data collection	*Provide details about the data collection procedure, including the instruments or devices used to record the data (e.g. pen and paper, computer, eye tracker, video or audio equipment) whether anyone was present besides the participant(s) and the researcher, and whether the researcher was blind to experimental condition and/or the study hypothesis during data collection.*
Timing	*Indicate the start and stop dates of data collection. If there is a gap between collection periods, state the dates for each sample cohort.*
Data exclusions	*If no data were excluded from the analyses, state so OR if data were excluded, provide the exact number of exclusions and the rationale behind them, indicating whether exclusion criteria were pre-established.*
Non-participation	*State how many participants dropped out/declined participation and the reason(s) given OR provide response rate OR state that no participants dropped out/declined participation.*
Randomization	*If participants were not allocated into experimental groups, state so OR describe how participants were allocated to groups, and if allocation was not random, describe how covariates were controlled.*

Ecological, evolutionary & environmental sciences study design

All studies must disclose on these points even when the disclosure is negative.

Study description	*Briefly describe the study. For quantitative data include treatment factors and interactions, design structure (e.g. factorial, nested, hierarchical), nature and number of experimental units and replicates.*
Research sample	*Describe the research sample (e.g. a group of tagged Passer domesticus, all Stenocereus thurberi within Organ Pipe Cactus National Monument), and provide a rationale for the sample choice. When relevant, describe the organism taxa, source, sex, age range and any manipulations. State what population the sample is meant to represent when applicable. For studies involving existing datasets, describe the data and its source.*
Sampling strategy	*Note the sampling procedure. Describe the statistical methods that were used to predetermine sample size OR if no sample-size calculation was performed, describe how sample sizes were chosen and provide a rationale for why these sample sizes are sufficient.*

Data collection	*Describe the data collection procedure, including who recorded the data and how.*
Timing and spatial scale	*Indicate the start and stop dates of data collection, noting the frequency and periodicity of sampling and providing a rationale for these choices. If there is a gap between collection periods, state the dates for each sample cohort. Specify the spatial scale from which the data are taken*
Data exclusions	*If no data were excluded from the analyses, state so OR if data were excluded, describe the exclusions and the rationale behind them, indicating whether exclusion criteria were pre-established.*
Reproducibility	*Describe the measures taken to verify the reproducibility of experimental findings. For each experiment, note whether any attempts to repeat the experiment failed OR state that all attempts to repeat the experiment were successful.*
Randomization	*Describe how samples/organisms/participants were allocated into groups. If allocation was not random, describe how covariates were controlled. If this is not relevant to your study, explain why.*
Blinding	*Describe the extent of blinding used during data acquisition and analysis. If blinding was not possible, describe why OR explain why blinding was not relevant to your study.*

Did the study involve field work? ☐ Yes ☒ No

Reporting for specific materials, systems and methods

We require information from authors about some types of materials, experimental systems and methods used in many studies. Here, indicate whether each material, system or method listed is relevant to your study. If you are not sure if a list item applies to your research, read the appropriate section before selecting a response.

Materials & experimental systems

n/a	Involved in the study
☒	☐ Antibodies
☒	☐ Eukaryotic cell lines
☒	☐ Palaeontology and archaeology
☒	☐ Animals and other organisms
☒	☐ Clinical data
☒	☐ Dual use research of concern

Methods

n/a	Involved in the study
☒	☐ ChIP-seq
☒	☐ Flow cytometry
☒	☐ MRI-based neuroimaging